Self-activated epitaxial growth of ScN films from molecular nitrogen at low temperatures

Cite as: APL Mater. 12, 111108 (2024); doi: 10.1063/5.0222995
Submitted: 11 June 2024 • Accepted: 23 October 2024 •
Published Online: 6 November 2024

Chandrashekhar P. Savant,[1,a] Anita Verma,[1] Thai-Son Nguyen,[1] Len van Deurzen,[2] Yu-Hsin Chen,[1] Zhiren He,[3] Salva S. Rezaie,[2,4] Jakob Gollwitzer,[1] Benjamin Gregory,[1] Suchismita Sarker,[5] Jacob Ruff,[5] Guru Khalsa,[3] Andrej Singer,[1] David A. Muller,[2,4] Huili G. Xing,[1,4,6] Debdeep Jena,[1,2,4,6] and Joseph Casamento[7,a),b)]

AFFILIATIONS

[1] Department of Materials Science and Engineering, Cornell University, Ithaca, New York 14853, USA
[2] School of Applied and Engineering Physics, Cornell University, Ithaca, New York 14853, USA
[3] Department of Physics, University of North Texas, Denton, Texas 76203, USA
[4] Kavli Institute at Cornell for Nanoscale Science, Cornell University, Ithaca, New York 14853, USA
[5] Cornell High Energy Synchrotron Source, Cornell University, Ithaca, New York 14853, USA
[6] School of Electrical and Computer Engineering, Cornell University, Ithaca, New York 14853, USA
[7] Department of Materials Science and Engineering, Massachusetts Institute of Technology, Cambridge, Massachusetts 02142, USA

[a)] **Authors to whom correspondence should be addressed:** cps259@cornell.edu and jac93@mit.edu
[b)] **Present address:** Department of Materials Science and Engineering, Massachusetts Institute of Technology, Cambridge, MA 02142, USA.

ABSTRACT

Unlike naturally occurring oxide crystals such as ruby and gemstones, there are no naturally occurring nitride crystals because the triple bond of the nitrogen molecule is one of the strongest bonds in nature. Here, we report that when the transition metal scandium is subjected to molecular nitrogen, it self-catalyzes to break the nitrogen triple bond to form highly crystalline layers of ScN, a semiconductor. This reaction proceeds even at room temperature. Self-activated ScN films have a twin cubic crystal structure, atomic layering, and electronic and optical properties comparable to plasma-based methods. We extend our research to showcase Sc's scavenging effect and demonstrate self-activated ScN growth under various growth conditions and on technologically significant substrates, such as 6H–SiC, AlN, and GaN. *Ab initio* calculations elucidate an energetically efficient pathway for the self-activated growth of crystalline ScN films from molecular N_2. The findings open a new pathway to ultralow-energy synthesis of crystalline nitride semiconductor layers and beyond.

I. INTRODUCTION

Although our atmosphere is 78.1% N_2 and 21% O_2, most of the earth's crust and naturally occurring compounds and minerals are oxides, not nitrides. This is because of the formidable strength of 9.8 eV/molecule of the N≡N triple bond in molecular N_2, one of the strongest bonds.[1] Lightning and nitrogenase enzymes are two primary mechanisms for breaking the N_2 triple bond in nature.[2] Electrical discharge in lightning generates the high energy needed to dissociate N_2 molecules, forming nitrogen oxides (NO_x) that contribute to nitrogen deposition in soils. Biological nitrogen fixation is driven by nitrogenase enzymes using energy-efficient processes to break the strong triple bond.[3] The transition metal Fe Mo cofactors in the nitrogenase catalyze the breaking of the strong triple bond of atmospheric N_2, thereby facilitating the binding, activation, and conversion of atmospheric N_2 into ammonia.[3,4] While natural lightning contributes, most natural nitrogen fixation on earth is efficiently driven by biological nitrogen-fixing micro-organisms

that carry out the process more efficiently, sustaining life on our planet.[5]

Although nature has a mechanism to dissociate atmospheric N_2, there is a dire need for a low-energy synthetic process to synthesize metal nitrides directly from N_2. At present, the synthesis of inorganic nitride crystalline compound metals and semiconductors that have revolutionized electronic and photonic devices relies on high-power plasma to break N_2 bonds akin to natural lightning or at high temperatures to dissociate NH_3. The insufficient reactivity of metal cations with nitrogen requires these epitaxial nitride heterostructures to be synthesized with low impurity levels by high-temperature processes (e.g., >700 °C) via metalorganic chemical vapor deposition (MOCVD) or plasma-assisted processes via molecular beam epitaxy (MBE) at moderate temperatures (e.g., 400–700 °C). While the high energy is necessary to promote crystallinity and to overcome the limited reactivity of metal and nitrogen, it also results in physical and chemical defects.[6–8] It also precludes their use in back-end-of-line (BEOL) semiconductor processing, which has a low thermal budget. The ability to deposit nitride materials by an energy-efficient, lower-temperature process will, therefore, create significant fundamental and technological opportunities.

While investigating the growth of the semiconductor ScN using a plasma-activated source of N_2, we have discovered to our surprise that crystalline layers of semiconducting ScN could be deposited *even when Sc is exposed to molecular* N_2, i.e., *without the plasma*. In this work, we describe this study of the synthesis of ScN by two processes: (a) in the presence of molecular nitrogen: an entirely thermal process (without nitrogen plasma), and (b) with a plasma-assisted process. Owing to a low electronegativity and small nuclear effective charge, Sc has a significant affinity to bond with anions such as oxygen and halogens, forming Sc_2O_3, ScF_3, and $ScCl_3$.[9] The heightened reactivity of Sc compared to Ga and Al posed the fundamental question if Sc-containing nitride thin films can be grown in a vastly different manner than the traditional methods. We observed a strong scavenging effect of scandium metal, highlighting its high reactivity toward nitrogen and oxygen, suggesting that scandium can promote self-activated epitaxial growth at BEOL-compatible temperatures without an active nitrogen species (i.e., the nitrogen plasma) to facilitate film growth. This mechanism differs entirely from the existing growth methods. We observe self-activated epitaxial ScN film growth under several growth conditions by varying the substrate temperature, Sc flux, and N_2 flow rate on various substrates of interest. Structural, optical, and physical properties of the ScN films grown from molecular N_2 show comparable or even better quality than those grown in the standard way with N_2 plasma. A possible energy-efficient pathway in which Sc facilitates the bond breaking of molecular N_2 leading to the growth of ScN films is identified by *ab initio* calculations. These findings open a new window for the low-energy synthesis of novel nitride heterostructures, integration schemes, and applications while enhancing our understanding of the synthesis of transition metal nitride compounds and, at the same time, suggesting a reinvestigation of the reactivity of metals with molecular nitrogen.

II. RESULTS

Metal nitrides, including transition metal nitrides (e.g., TiN and TaN) and group-III semiconductor nitrides (e.g., GaN and AlN), are of great technological significance. Their mechanical, thermal, optical, and electronic properties enable a pivotal role in solid-state lighting, acoustic devices, and high-power electronic applications in laser diodes, RF power amplifiers, and acoustic wave resonators for 5G and 6G technologies.[10–13] Being a transition metal nitride, scandium nitride (ScN) possesses an excellent hardness of ~21 GPa,[14] an elastic modulus of ~356 GPa,[14] a high melting point of ~2600 °C,[14,15] and thermal stability.[15–17] Furthermore, ScN is a semiconductor with an energy bandgap of ~1.3 eV and can be doped n-type and p-type.[18] ScN also possesses a high Seebeck coefficient of $\sim -86\ \mu\ VK^{-1}$ and a high thermoelectric power factor of $2.5 \times 10^{-3}\ Wm^{-1}\ K^{-2}$ at 800 K, surpassing commercially available PbTe.[15,18] Cubic ScN (111) has <0.1% lattice mismatch with wurtzite GaN (0001), enabling the utilization of ScN for dislocation reduction, *in situ* Ohmic contacts, and current spreading layers in GaN-based devices.[19–25] The giant polarization discontinuity of ScN with other group-III nitrides is predicted to make it a suitable candidate for polarization-enhanced tunnel junctions.[26] Incorporation of ScN and alloying nitrides with Sc promises to bring to the established group-III nitride (GaN, AlN, and InN) based electronics and photonics family previously missing properties such as thermoelectric,[15,18] plasmonic,[27] extremely high piezoelectric,[28–30] ferroelectric,[31–34] and high dielectric constant[30] behavior.

The ScN films in this study were grown in a molecular beam epitaxy system with and without striking nitrogen plasma from molecular N_2 on 6H–SiC substrates to assess the reactivity of Sc with molecular nitrogen and to assess the feasibility of self-activated growth. Figure 1(a) shows the *in situ* reflection high-energy electron diffraction (RHEED) pattern of ScN films grown at 550 °C with nitrogen plasma (left) and without nitrogen plasma (right). These diffraction patterns after 40 min of growth [Fig. 1(a); A_1 and A_2] indicate rotated domains with two separate overlaid $\langle 1\bar{1}0 \rangle$ zone axes, indexed as pairs of {111} and {002} families of planes, as indexed by red and blue colors on the RHEED pattern. ScN films grown without plasma at different substrate temperatures of 20, 350, 750, and 950 °C show a similar RHEED diffraction pattern [Fig. S1(a)]. As illustrated in Fig. 1(a), all RHEED patterns signify twin cubic ScN film growth of similar character, with and without striking plasma. Figure 1(b) illustrates a ScN/6H–SiC structural schematic showing $\langle 111 \rangle$ oriented ScN film with two 60° oriented twin domains of ScN framed in blue and red colors on a $\langle 0001 \rangle$ oriented 6H–SiC substrate. Along the [0001] direction of 6H–SiC, (111) cubic twin ScN domains form instead of a pure hexagonal, wurtzite, or zinc blende phase due to the thermodynamic stability of the rock salt cubic structure of ScN.[25,35–38]

Twin domains are expected to result from the symmetry constraints encountered upon growing a three-fold symmetric cubic crystal on a six-fold symmetric hexagonal substrate.[25] After extended growths of ~135 min, polycrystalline rings appear in the diffraction pattern for the ScN film grown with plasma, as shown in Fig. 1 A_3. In contrast, the spotty twin domain diffraction pattern of ScN films persists for the ScN film grown without plasma, as shown in Fig. 1 A_4. This indicates that thicker ScN films grown without plasma have a high crystalline quality and maintain an excellent epitaxial registry with the substrate.

Bulk structural properties were analyzed using lab-based and synchrotron x-ray diffraction. Figures 1(c)–1(e) show the crystalline phase, orientation, and epitaxial registry of the ScN film grown

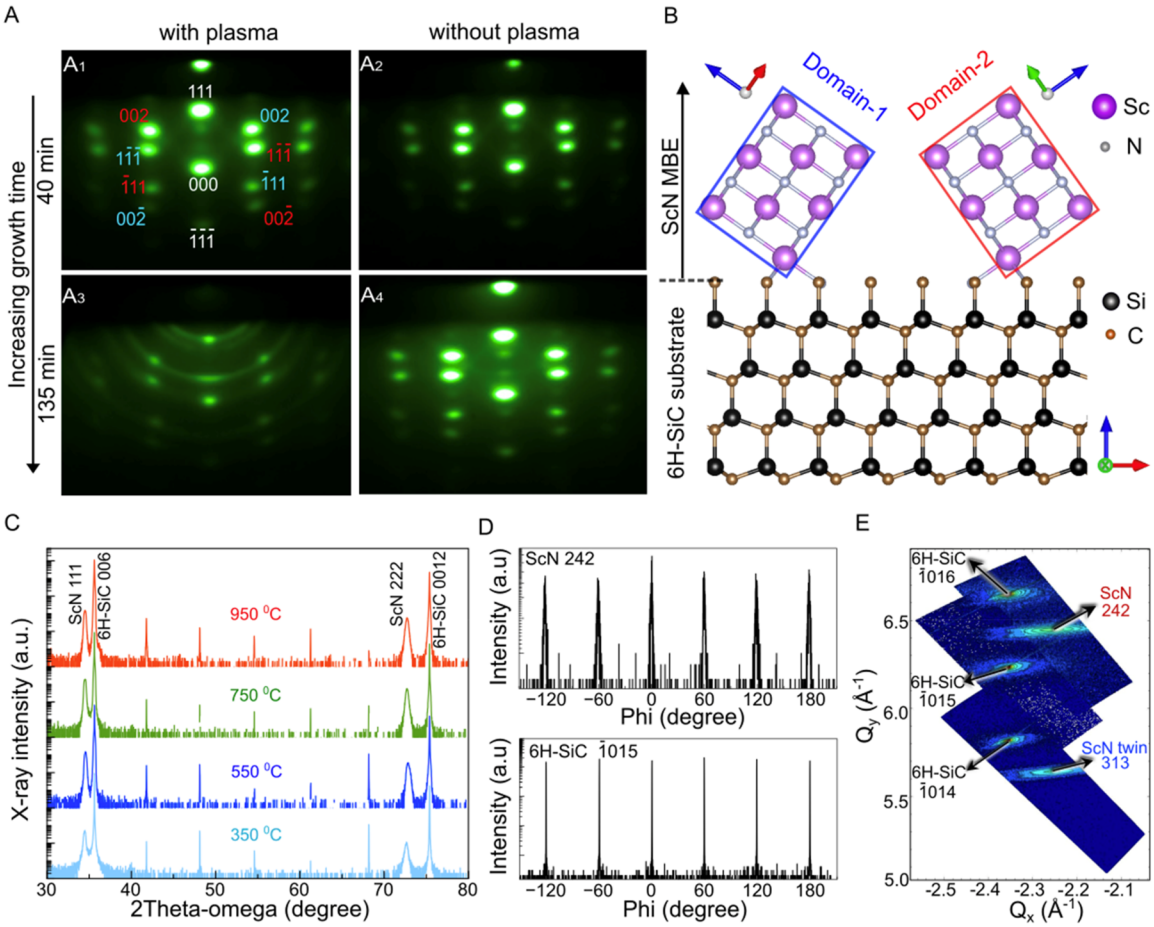

FIG. 1. Diffraction studies (RHEED, XRD) showing twinned cubic ScN film growth and epitaxial registry with the 6H–SiC substrate. (a) Reflection high-electron diffraction (RHEED) pattern of ScN films collected at 40 min, ~88 nm of growth (top, A_1, A_2) and 135 min, ~294 nm of growth (bottom, A_3, A_4) on Si-face 6H–SiC substrate at 550 °C substrate temperature, and Sc flux of 2.5×10^{-8} Torr with plasma (left, A_1, A_3) and without plasma (right, A_2, A_4). Red and blue indices show diffraction patterns from each domain, and the white index shows overlapping peaks from each domain. (b) ScN/6H–SiC structural schematic showing crystallographic orientations of twin domains of cubic ScN with respect to the 6H–SiC substrate; twin domains of ScN are framed in red and blue. (c) X-ray diffraction spectra of ScN films grown without plasma on 6H–SiC substrates at different substrate temperatures (350, 550, 750, and 950 °C) showing cubic ScN growth epitaxially in (111) orientation. (d) Skew-symmetric phi (Φ) scans of ScN 242, 6H–SiC $\bar{1}015$ reflections for ScN films grown without plasma at 550 °C. (e) Reciprocal space maps of ScN, 6H–SiC reflections for ScN films grown without plasma at 550 °C indicating epitaxial film registry with 6H–SiC substrate.

without plasma assessed using x-ray diffraction (XRD). The ScN 111 and 222 reflections were observed [Fig. 1(c) and S1(b)] for ScN films grown without plasma at substrate temperatures from 20 to 950 °C. To test for the in-plane epitaxial relationship between ScN and the substrate, skew-geometry phi-scans of asymmetric ScN 242 and 6H–SiC $\bar{1}015$ reflections are shown in Fig. 1(d). Six peaks at the same positions indicate the six-fold symmetry[14,25] and the epitaxial registry of the ScN films with 6H–SiC substrate. The full-width-half-maximum (FWHM) of the individual peaks in the ScN 242 phi scan are ~0.5°, indicating a high degree of in-plane orientation. Similar six-fold symmetry and epitaxial registry were also observed for the ScN films grown with plasma.[25]

Figure 1(e) shows a reciprocal space map (RSM) of 6H–SiC and twin-cubic ScN asymmetric reflections, i.e., 242 from the first domain and 313 from the second twin domain, for ScN grown from molecular N_2 without plasma. No metallic Sc peaks were observed in the reciprocal space maps. The XRD-RSM confirms the high reactivity of Sc with diatomic nitrogen, the growth of (111) ScN films with cubic twin domains over a wide substrate temperature range from 20 to 950 °C without plasma, and its epitaxial growth registry with 6H–SiC substrate. Similar twinned-cubic ScN film growth using molecular N_2 without nitrogen plasma was also observed on other wurtzite (0002) oriented substrates such as GaN and AlN (see the supplementary material).

There is a possibility that a small fraction of Sc flux does not form ScN and remains as a secondary phase of metallic Sc. Such metallic inclusions are undesirable in semiconducting ScN. Lab-source XRD has limited x-ray energies and detection range, making

the detection of small fractions of secondary phases challenging. To remedy this, a large volume of the 3D reciprocal space was measured using synchrotron x-ray scattering to detect residual unreacted Sc in the ScN film.

Figures 2(a) and 2(b) show 2D slices of experimentally measured 3D RSMs in the H = 0 plane for the ScN thin films grown with plasma, and without plasma on a 6H–SiC substrate. Figure 2(c) (For more information, please see Figs. S2–S4 of the supplementary material) shows a simulated RSM including 6H–SiC substrate (stars), a most likely Sc-metal inclusion phase (circles), and twinned cubic ScN domains (triangles). The comparison between the simulation [Fig. 2(c), S2(a)–(b), and S3(a)–(b)] and the data confirm that the observed experimental Bragg reflections measured by the x-ray scattering [Figs. 2(a) and 2(b), S2(d), and S3(d)–(e)] originate from twinned-cubic ScN thin film and 6H–SiC substrate, whereas no Sc-inclusion was observed. Furthermore, extensive phase purity analysis is performed by analyzing the entire large volume of the reciprocal space (Fig. S4), and no Bragg reflections are observed for any trace of secondary phases, such as metallic scandium or layered hexagonal ScN, etc., within the large volume of reciprocal space. This confirms the growth of phase pure twin cubic ScN films from molecular N_2 without plasma.

The atomic layer stacking of different twin ScN domains was analyzed using 3D RSM slices at different L-planes (see Fig. S3 of the supplementary material for details). The ScN thin films have a well-ordered crystal lattice with six-fold symmetry, with discrete ABCA atomic layer stacking from some twin domains and ACBA stacking from others. ScN film grown at 550 °C without plasma exhibits an intense peak with a low FWHM of 0.0865 r.l.u. (relative lattice units) in the out-of-plane direction, as shown in inset Fig. 2(b) (and Fig. S5). Intense ScN Bragg reflection peak [Fig. 2(b) and Fig. S5] with low FWHM indicates that the epitaxial ScN thin film grown without plasma is highly crystalline. Thus, ScN films with high crystal quality can be obtained in the explored growth parameter space (see the supplementary material), even in the absence of plasma, indicating the beneficial effects of self-activated growth.

Figures 3(a)–3(e) shows HAADF-STEM images of (111) ScN films grown on (0001) 6H–SiC substrates, highlighting distinct features between films grown with plasma (a) and (b), and without plasma (c)–(e). EDX spectra, shown in Fig. S6, validate N incorporation in the ScN films grown without plasma and demonstrate a uniform distribution of Sc and N throughout the film. The top surface of the ScN film grown without plasma [Fig. 3(c) and S7] exhibits a notable surface morphology characterized by sharp pyramid structures of ~18 nm height with {001} facets, providing clear evidence of columnar growth. As highlighted by alternating dark and bright contrasts in [Fig. 3(c) and S7], these columnar twin domains are rotated by 60° along [111] growth direction. Rotated twin domain formation

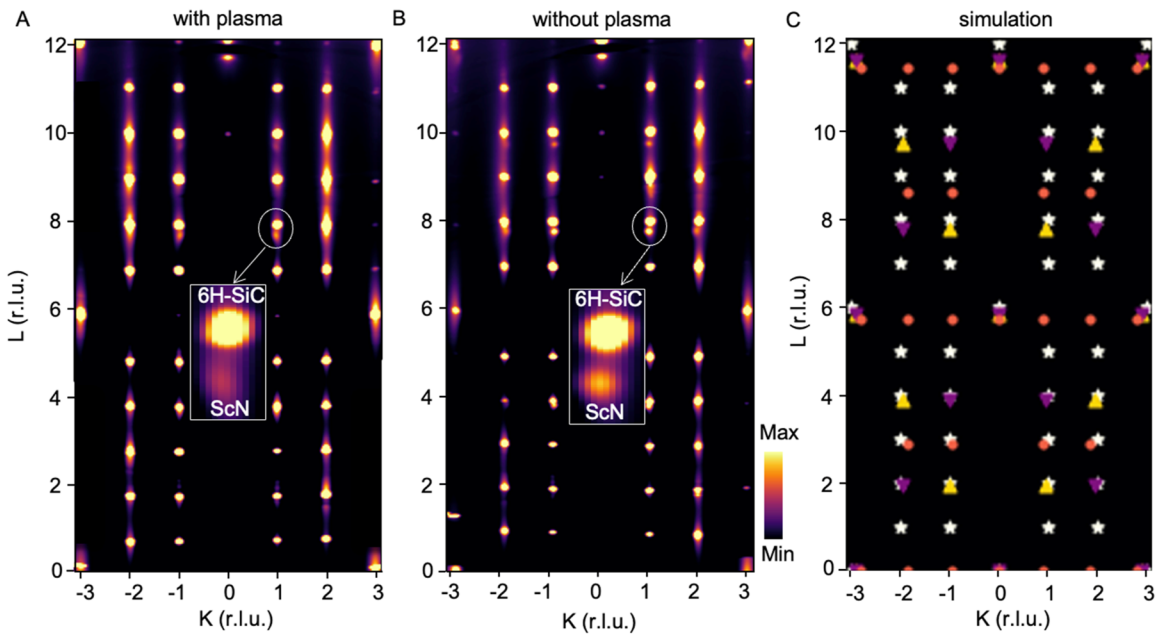

FIG. 2. Synchrotron source measured reciprocal space maps for ScN thin films and 6H–SiC substrates with theoretical simulation. 2D slices of 3D reciprocal space maps measured at QM2 beamline at CHESS enclosing multiple Bragg reflections related to ScN thin film twinned cubic crystal structure and 6H–SiC substrate hexagonal crystal structure in H = 0 plane for (a) ScN film grown with plasma at 550 °C and (b) ScN film grown without plasma at 550 °C. The data are indexed with respect to the 6H–SiC substrate lattice parameters, and the intensity of all Bragg peaks is shown on a logarithmic scale. Inset Figs. 2(a) and 2(b) show the ScN thin-film's and 6H–SiC substrate's Bragg reflections. Strong and intense ScN Bragg peaks indicate a high crystallinity of the ScN film grown without plasma. (c) The simulated diffraction pattern generated from the standard Crystallographic Information File for 6H–SiC substrate (white stars, space group: $P6_3mc$, [0001] out-of-plane, and $[01\bar{1}0]$ in-plane orientation), twinned ScN (triangles; space group: $Fm\bar{3}m$, [111] out-of-plane and $[2\bar{1}\bar{1}]$ (yellow up triangles) in-plane orientation; and [111] out-of-plane and $[\bar{2}11]$ (purple down triangles) in-plane orientation), Sc (red circles, space group: $P6_3/mmc$, [0001] out-of-plane and $[01\bar{1}0]$ in-plane orientation) by using the x-ray utility tool.[39]

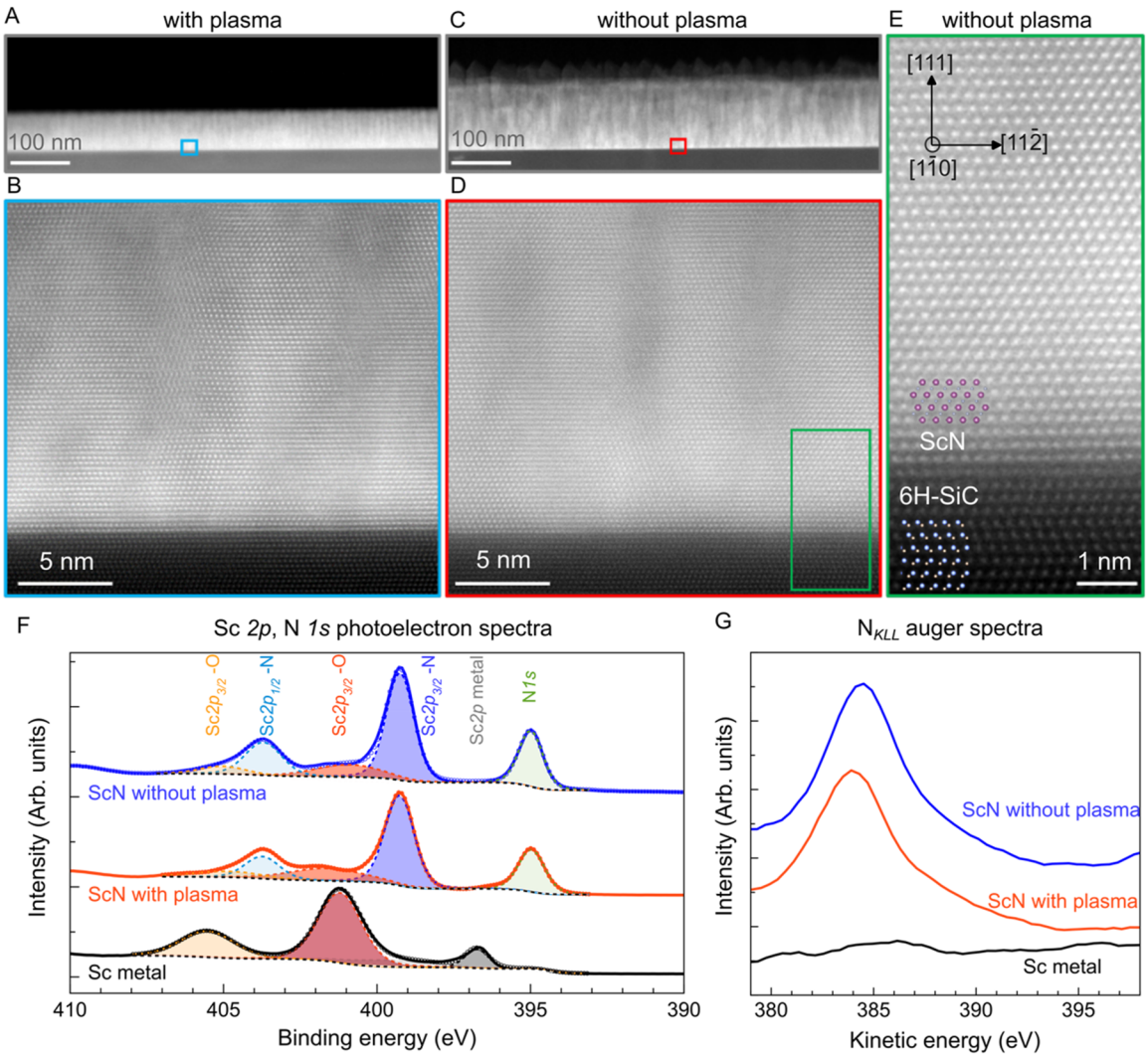

FIG. 3. Microstructure and composition analysis of ScN films using HAADF-STEM, XPS. (a) and (b) HAADF-STEM micrographs of ScN film grown with plasma; (c)–(e) ScN film grown without plasma at different magnifications, showing columnar grain growth of ScN, zig-zag facet surface from twinned cubic domains, and two different domains in ScN films; (f) XPS Sc2p, N1s core level photoelectron spectra; and (g) N_{KLL} Auger electron spectra for ScN film grown without plasma, ScN film grown with plasma, and metallic Sc film verifying the Sc–N bonding and the presence of nitrogen in the ScN films grown without plasma.

is an expected growth feature for cubic crystal growth on hexagonal (wurtzite) crystals, e.g., 6H–SiC, GaN, and AlN.[21]

Although STEM micrographs of ScN films grown with and without plasma indicate similar columnar growth, the microstructure differs. Notably, films grown without plasma show large domains extending from the substrate surface to the top of the film [Figs. 3(c) and 3(d) and S7D], leading to a sharp pyramidal morphology [Fig. S7(b)]. In contrast, films grown with plasma display smaller rotated domains [Fig. 3(b) and S7(c)], contributing to a smoother surface morphology [Fig. 3(a) and S7(a)]. The presence of these smaller rotated domains in films grown with plasma suggests a potential influence of plasma on the growth dynamics governing both domain size and orientation. The distinct characteristics observed in films grown without plasma, such as larger continuous domains and well-defined columnar structures, suggest a more controlled and organized growth process in the absence of plasma-induced effects. Figures S7 and S8 provide insights into the observed structural features by showcasing additional regions of films grown with and without plasma.

A high-resolution HAADF-STEM image of ScN film grown without plasma [Fig. 3(e)] shows the nominal structure of cubic ScN projected along $\langle 1\bar{1}0 \rangle$ direction. The interface between ScN and substrate is sharp, and the film has a coherent interface with the substrate. The ScN lattice constant obtained from the fast Fourier transform of this region and another region shown in Fig. S9 is ~4.3 Å, smaller than the relaxed lattice constant of 4.5 Å.[18,21,25]

The TEM FFT determined lattice parameter of ScN film close to the ScN/SiC interface is ~4.3 Å, corresponding to the in-plane spacing of ~4.3 × $\sqrt{2}$ = 3.05 Å within the (111) crystallographic plane. This value is close to the in-plane lattice parameter of SiC–6H ~3.07 Å, suggesting that the epitaxial ScN film at the ScN/SiC interface is pseudomorphically strained to the SiC–6H substrate. The bulk of the ~130–400 nm ScN films are relaxed, as observed from the XRD 111 Bragg reflection measured lattice constant of ~4.5 Å.

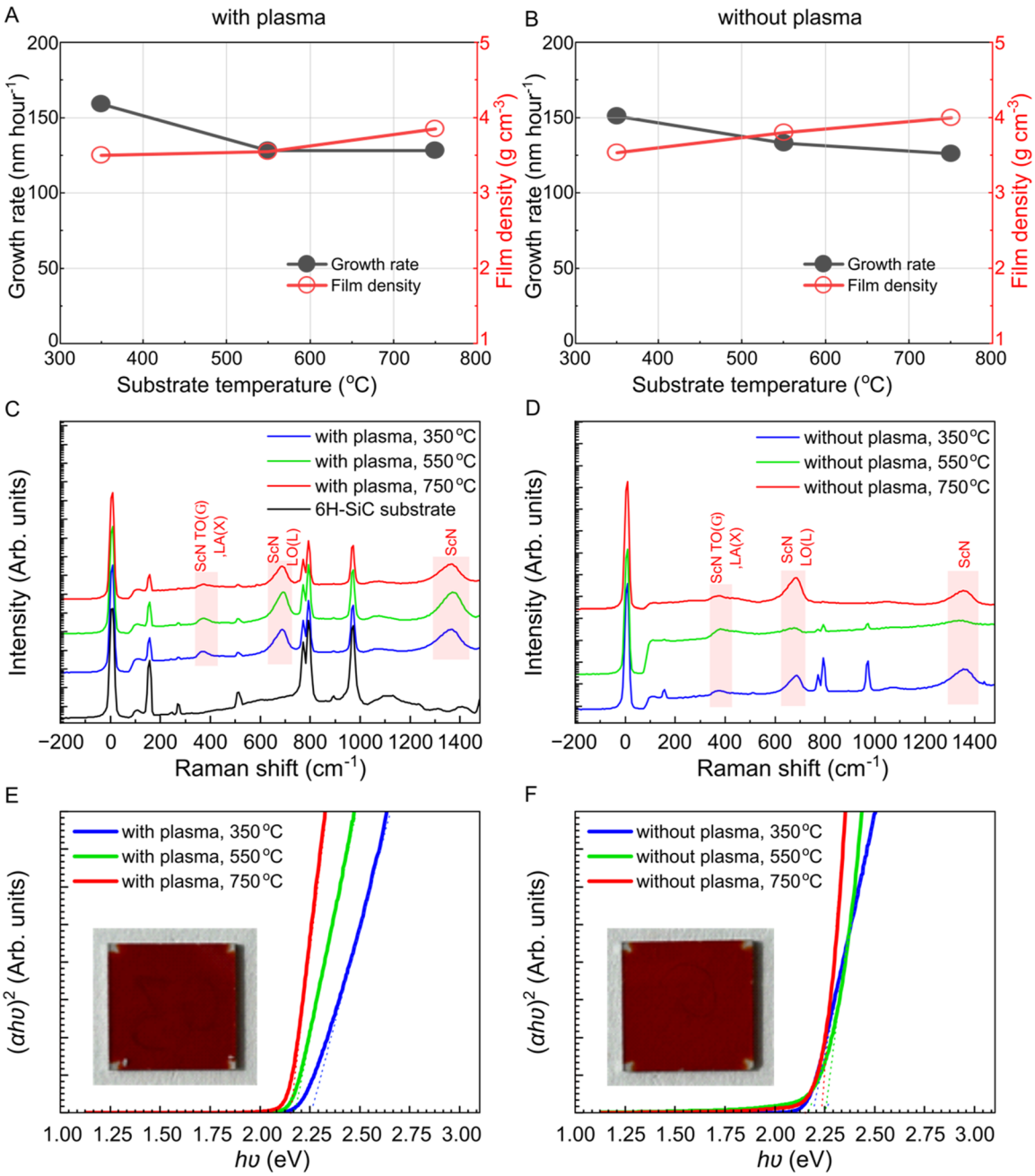

FIG. 4. Growth rate and properties (density, chemical bonding, and optical absorption) of ScN film. (a) and (b) Growth rates and densities of ScN films grown at different substrate thermocouple temperatures with plasma and without plasma, respectively, showing comparable growth rates and densities. (c) and (d) Raman spectra of cubic ScN films grown on 6H–SiC substrates at different substrate temperatures with plasma and without plasma, respectively, showing similar cubic ScN bonding in films grown. (e) and (f) Tauc plots from UV-visible absorption spectra for ScN films grown with plasma and without plasma show comparable absorption band edges. Insets of (e) and (f) show optical images of the representative ScN film samples grown at 550 °C substrate temperature.

Chemical bonding in the ScN films was analyzed using Sc2p, N1s core level x-ray photoelectron spectra [Fig. 3(f)], and N_{KLL} Auger electron spectra [Fig. 3(g)]. For reference, a metallic Sc film was used (see the Appendix for growth details). Deconvoluted peaks in the Sc2p core level photoelectron spectra in Fig. 3(f) indicate Sc–N bonding in the ScN film samples grown without plasma and with plasma. Unlike the metallic Sc film sample, metallic Sc–Sc bonding peaks were not evident in the ScN film samples. Sc–O bonding is apparent in all samples, likely from the surface oxidation. N1s core level photoelectron spectra and the N_{KLL} Auger electron spectra in Fig. 3(g) confirm the presence of nitrogen in the ScN films. A comparable [Sc]/[N] ratio of ~1.07 for the ScN films grown with plasma and ~1.13 for ScN films grown without plasma was observed by x-ray photoelectron spectroscopy (XPS).

The ScN film thickness and density were measured using x-ray reflectivity (XRR) to examine potential differences in ScN growth kinetics with and without plasma. Growth rates and densities of ScN films grown with and without plasma at varying growth temperatures are shown in Figs. 4(a) and 4(b). The films were grown in heavily nitrogen-rich conditions where Sc flux < N^* flux < N_2 flux in all cases of film growth presented here. Comparable growth rates with and without plasma indicate that the ScN growth is not limited by the availability of active N^* species but by the flux of Sc and is self-activated. Furthermore, the ScN growth rate is found to be dependent on the Sc flux rather than the N_2 flow rate, confirming that the self-activated ScN growth is not constrained by the availability of active N species. The ScN growth rate decreases from ~150 nm h^{-1} to ~125 nm h^{-1} as substrate temperature is increased from 350 to 750 °C. Increasing the growth temperature from 350 to 750 °C enhances the density of ScN films from ~3.6 to ~3.9 g cm^{-3}, potentially facilitated by higher adatom surface mobility promoted by elevated substrate temperature or changes in surface growth kinetics at higher temperatures.[40–43]

Figures 4(c) and 4(d) show the Raman spectra of the ScN films and 6H–SiC substrate for reference. Distinct from 6H–SiC Raman peaks, we observe additional Raman peaks at ~365, ~683, and ~1355 cm^{-1}. The Raman peaks at ~365 cm^{-1} correspond to the cubic ScN TO(Γ) and LA(X) modes, and at ~683 cm^{-1} correspond to the cubic ScN LO(L) mode.[20,44,45] A cubic ScN second-order peak appears at ~1300 to 1360 cm^{-1}.[20] The Raman peaks for ScN films grown without and with nitrogen plasma are at comparable wavenumbers, indicating similar Sc–N bonding.

Rock-salt crystalline ScN is a semiconductor. The energy bandstructure has a valence band maximum at the Γ-point and a conduction band minimum at the X-point, with an indirect gap in the range of 0.9–1.6 eV corresponding to the $\Gamma \rightarrow X$ transition and a direct gap of ~2.1–2.4 eV corresponding to the transition at the X point.[14,46,47] The measured Tauc plots for ~300 nm thick ScN films grown with plasma are shown in Fig. 4(e), and those for ~400 nm thick ScN films grown without plasma are shown in Fig. 4(f). The extracted optical absorption edge values of ~2.20 (+/−0.05) eV for all ScN samples align closely with reported values for degenerately doped ScN films.[14,46,47] In Figs. 4(e) and 4(f), insets display brown–orange-colored ScN film samples, matching the simulated color (Fig. S10) of uniformly integrated 740 to 565 nm, 1.68–2.2 eV light, indicative of ScN's transparency window in the visible regime. The ScN films grown with and without plasma show similar transport properties with comparable electron carrier concentrations of

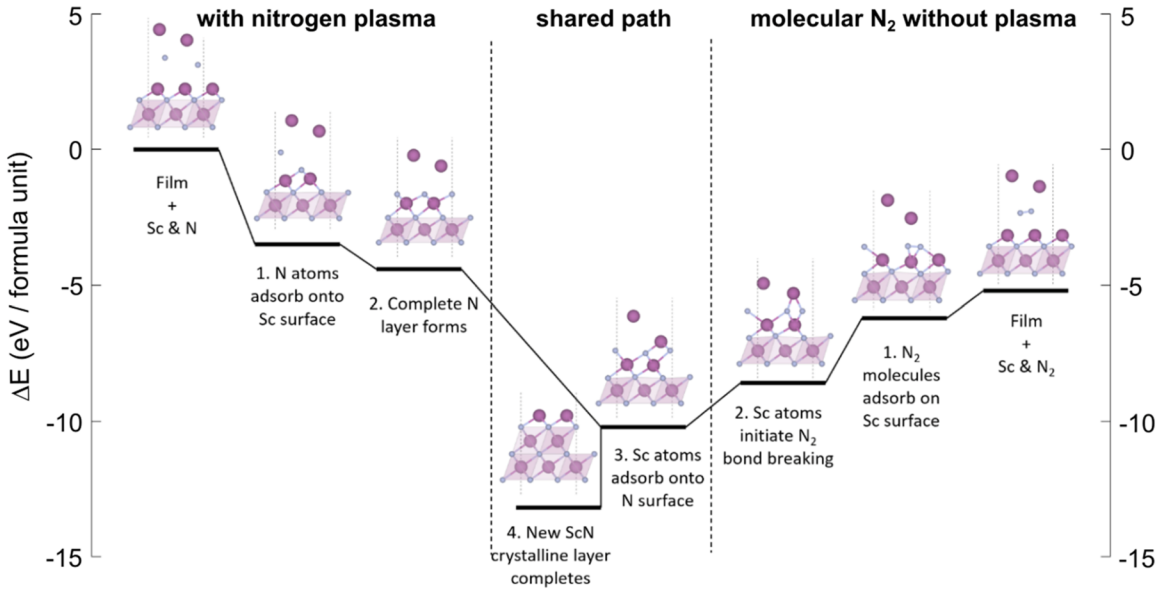

FIG. 5. *Ab initio* ScN growth pathways. The nitrogen plasma growth pathway (left) begins with the adsorption of individual N atoms, forming a N layer in a region of the Sc-terminated surface. The molecular nitrogen growth pathway (right) begins with the adsorption of N_2 molecules in a region of the Sc-terminate surface. Sc atoms then facilitate the breaking of the N_2 bond on the surface. The two growth pathways converge (center) during the adsorption of Sc atoms to complete the growth of a new ScN layer.

~1.5 × 10^{19} to 8 × 10^{20} cm^{-3} and Hall mobilities of ~1–5 cm^2/V.s (Fig. S11). As observed in XPS, the as-grown ScN films are inherently n-type due to O impurity doping. Comparable optical absorption edges and transport properties in ScN films grown with and without plasma suggest that plasma-free growth is a viable method for obtaining semiconducting ScN films for electronic and photonic applications.

To study the similarities between growth with and without plasma, the possible paths for growth with nitrogen plasma and molecular N_2 are studied via density functional theory (DFT) calculations. For each case, a path that builds one complete ScN layer, connected by several intermediate metastable states that successively lower the energy is identified and summarized in Fig. 5. The total energy is found by summing up the energies of the slab, including any adsorbed atoms/molecules, with the remaining isolated atoms (or molecules), where the nitrogen plasmas are approximated as nitrogen atoms (see the Appendix). Our calculations reveal a large energetic push toward the formation of additional ScN layers. With respect to the reference energies for nitrogen plasma and molecular N_2 growth, a 13.2 eV/formula unit (nitrogen plasma) and 8.0 eV/formula unit (molecular N_2) energy decrease is found. This shows that both processes are highly exothermic, which agrees with the lower growth rate at higher substrate temperatures. Moreover, our nudged elastic band calculations indicate no energy barriers along both paths (see Figs. S12 and S13).

For the growth process with nitrogen plasma, we find a direct path to the growth of additional ScN layers. Starting with a Sc-terminated surface, nitrogen atoms are adsorbed to form a N-terminated surface (Fig. 5; left, steps 1–2). After that, the adsorption of Sc atoms completes the new crystalline layer (Fig. 5; center, steps 3–4). For molecular N_2 growth, the initial process (Fig. 5; right, steps 1–3) is different, converging to a shared path with nitrogen plasma in the final step. First, a nitrogen molecule binds onto the Sc-terminated surface (Fig. 5; right, step 1). However, in contrast to the nitrogen plasma pathway, a complete N layer cannot be formed without the assistance of a Sc atom. Once a Sc atom lands on top of the adsorbed surface N_2, the surface structure experiences large distortions that involve a significant increase in the N–N bond length, forming a N layer with partial Sc coverage (Fig. 5; right, steps 2–3). Finally, additional Sc atoms fall onto the surface to complete the layer.

To evaluate the reactive nature of Sc, we studied its gettering or scavenging effect by evaporating scandium from a Knudsen effusion cell at 1408 °C with a Sc beam equivalent flux of 3 × 10^{-8} Torr. The chamber base pressure remained constant before opening the Sc effusion cell shutter. As shown in Fig. S14(a), upon opening the shutter, the MBE chamber pressure immediately dropped (t = 0 min), indicating a gettering effect as Sc captured residual species. Monitoring gas partial pressures with a residual gas analyzer (RGA) during 80 min of Sc exposure revealed a rapid decrease in the first 10 min and subsequent decay [Fig. S14(b)]. After Sc exposure, the RGA mass spectra [Fig. S14(c)] displayed reduced partial pressures of residual gas species (notably, H_2 and $^{14}N_2$), highlighting Sc's scavenging capabilities. This behavior, similar to titanium sublimation pumps in ultra-high vacuum systems, showcases Sc's high reactivity. Notably, such pressure reduction was not observed when opening Al, Ga, and In shutters, emphasizing Sc's distinct gettering behavior.

Self-activated ScN films were also grown on other technologically relevant substrates, such as (0001) oriented AlN and GaN. RHEED and XRD diffraction patterns [Figs. S15(a) and (c)] show twin cubic ScN (111) film growth on AlN and GaN substrates, akin to 6H–SiC. AFM micrographs [Fig. S15(b)] of ~120–150 nm thick ScN films grown without plasma reveal a surface roughness of ~2–3.3 nm, aligning with ScN film morphology on 6H–SiC substrate. The ScN film growth rate on GaN, AlN, and 6H–SiC substrates was 97.5, 112, and 133 nm h^{-1}, respectively, under the same source fluxes, and the corresponding film densities were 4.0, 3.88, and 3.8 g cm^{-3}, correlating with the substrate thermal conductivity. GaN, 130 Wm^{-1} K^{-1} < AlN, 350 Wm^{-1} K^{-1} < 6H–SiC, 490 Wm^{-1} K^{-1} and in-plane lattice mismatch with substrate: GaN, −0.1% < AlN, 2.3% < 6H–SiC, 3.4%. Self-activated growth of ScN is likely exothermic. As shown in Figs. 4(a) and 4(b), the higher substrate temperature results in a lower growth rate and higher density of ScN films. Similarly, a substrate with relatively lower thermal conductivity (e.g., GaN) will have higher surface temperatures due to poor heat dissipation, leading to a lower growth rate, possibly due to finite decomposition/thermal desorption of Sc and ScN, and a higher film density due to higher adatom mobility and annealing effects.[40,41] In addition, it is possible that different growth rates, reaction kinetics on different substrates, as well as a different lattice mismatch with the substrate, would lead to varying densities of the ScN films.[40–43]

In addition, Sc flux and nitrogen flow rates were varied during self-activated growth to understand the growth-limiting species during the ScN growth kinetics. As shown in Table-S2, at a constant nitrogen flow rate of 3.3 standard cubic centimeters per minute (sccm), the ScN film growth rates increase from 17 to 151 nm h^{-1}, with increasing Sc flux from 0.8 × 10^{-8} to 3 × 10^{-8} Torr. Conversely, at a constant Sc flux (of 3 × 10^{-8} Torr), the ScN film growth rate remains constant over an extensive range of N_2 flow rates from 1.08 to 3 sccm. This indicates that ScN growth rates are Sc flux-limited rather than constrained by the availability of active N species.

III. DISCUSSION

Because the conventional inorganic synthesis of epitaxial nitrides relies on high-power plasma to break N_2 bonds, our report of the self-activated energy-efficient synthesis of crystalline ScN films directly from molecular N_2 bypasses the need for high-temperature reactions or energetic plasma discharge. The findings have significant implications for fundamental thin film deposition and making integration of electronic, photonic, acoustic, and quantum devices possible in configurations that were ruled out before.

The self-activated growth method reported here is significant because (1) it challenges the conventional paradigms in nitride semiconductor synthesis, offering new growth regimes and opportunities for heterogeneous integration of different material platforms and technologies. For instance, the high-temperature processes traditionally required for growing nitrides as active layers in electronic and photonic devices are incompatible with the back-end-of-line (BEOL) semiconductor processing, precluding straightforward CMOS integration of most nitrides. The ability to grow high-quality nitrides with BEOL-compatible semiconductor processing temperatures opens new opportunities for heterogeneous BEOL

integration of these nitrides in existing CMOS technologies. (2) The findings offer an energy-efficient nitride semiconductor synthesis route, potentially lowering manufacturing costs and environmental impact. (3) The self-activated growth of nitrides utilizes molecular N_2, which is abundant in the atmosphere, eliminating the need for costly precursors such as NH_3, hydrazine, methyl amines, etc. (4) Self-activation growth kinetics and synthesis parameters showcase the versatility of self-activated growth on various technologically significant substrates such as 6H–SiC, AlN, and GaN. The observation of phase-pure semiconducting ScN with atomic layering exhibiting epitaxial registry, sharp, coherent interfaces with the substrate, and larger continuous domains and well-defined columnar grain structures suggests that self-activated grown layers lead to higher quality layer growth without plasma-induced effects.

The observation of a substantial reactivity of scandium with molecular N_2 and other residual gas species, coupled with the theoretical insights elucidating the energetically efficient pathway for the self-activated growth of nitride films from molecular N_2, expands our understanding of transition metal nitrides and their synthesis route and motivates similar searches in other transition metals also such as Ti, Nb, Y, W, Mo, Zr, La, etc. that show scavenging effects.[48,49] This strategy can potentially be extended for the epitaxial growth of other transition metal nitrides (YN, NbN, TiN, TaN, ZrN, etc.) and rare earth nitrides (LaN, LuN, etc.) that host metallic, superconducting, semiconducting, magnetic, and piezoelectric properties. Owing to its scavenging nature, scandium can potentially be considered in sublimation pumps where Ti is currently used.[48,49] In addition to the several opportunities in electronic, photonic, electroacoustic, and quantum device applications mentioned earlier, the ability of Sc and related metals to self-catalyze growth could be exploited to enable new pathways for the synthesis of other nitride materials that are currently not possible because of the 9.8 eV high energy barrier of the N≡N triple bond in molecular N_2.

IV. CONCLUSION

In conclusion, self-activated epitaxial growth of crystalline, phase-pure, semiconducting ScN thin films has been demonstrated from molecular N_2 without plasma and at temperatures compatible with back-end-of-line semiconductor processing (<400 °C). The ability to grow phase pure ScN epitaxially with six-fold rotational symmetry on 6H–SiC substrates with excellent crystallinity, comparable bonding, and a direct bandgap of 2.2 eV (due to degenerate doping) without plasma activation and at temperatures as low as 20 °C results in a completely different paradigm for nitride semiconductors. The observation that Sc itself can break N_2 bonds with little thermal assistance opens the synthesis and processing space for transition metal nitrides. It challenges the accepted notion that high temperatures and plasma assistance are unavoidable for the growth of transition metal nitrides and their alloys. This has significant implications for energy-efficient processing and for advancing the transition metal nitrides in pioneering devices.

SUPPLEMENTARY MATERIAL

Additional data that support the findings of this work are provided in the supplementary material, which includes synchrotron-measured RSMs, diffraction simulations, atomic layering sequences in twin cubic films, and extensive phase purity analysis. HAADF STEM, EDAX and FFT data, Hall measurements, and *Ab initio* calculations are also provided together with the scavenging effect of Sc on residual species and the self-activated ScN growth demonstration at different growth temperatures, substrates, and N_2, Sc fluxes.

ACKNOWLEDGMENTS

This work was partly supported by SUPREME, one of seven centers in JUMP 2.0, a Semiconductor Research Corporation (SRC) program sponsored by DARPA. This work made use of a Helios FIB supported by NSF (Grant No. DMR-1539918) and the Cornell Center for Materials Research (CCMR) Shared Facilities, which are supported through the NSF MRSEC Program (Grant No. DMR-1719875). The Thermo Fisher Spectra 300 X-CFEG was acquired with support from PARADIM (NSF MIP DMR-2039380) and Cornell University. S.S.-R. acknowledges the support of the Kavli and PARADIM fellowships. A.V., J.G., B. G., and A.S. acknowledge the support of the U.S. Department of Energy, Office of Science, Office of Basic Energy Sciences, under Contract No. DE-SC0019414 (synchrotron x-ray characterization). This work was also performed in part at the Cornell NanoScale Facility, a member of the National Nanotechnology Coordinated Infrastructure (NNCI), which was supported by the National Science Foundation (Grant No. NNCI-1542081). The National Science Foundation (BIO, ENG, and MPS Directorates) supports research conducted at the Center for High-Energy X-ray Science (CHEXS) under award no. DMR-1829070.

AUTHOR DECLARATIONS

Conflict of Interest

The authors have no conflicts to disclose.

Author Contributions

The thin-film growth, measurements, and structural analysis were performed by C.S. The thin-film growths were performed by C.S. and T.N. XRR measurements were performed by C.S., T.S., and Y.C., A.V., C.S., S.S., J.R., J.G., and B.G. performed synchrotron diffraction measurements. The synchrotron data were analyzed by A.V. with the help of A.S. and C.S. The STEM investigations were carried out by S.S.R. and D.M. Optical measurements were performed by L.v.D., and C.S., G.K., and Z.H. performed the first principles calculations. All authors discussed the results. C.S., J.C., A.V., and G.K., contributed to writing the article. J.C. designed the experiment with C.S. and jointly supervised the work with H.G.X. and D.J.

Chandrashekhar P. Savant: Conceptualization (equal); Data curation (equal); Formal analysis (equal); Investigation (equal); Methodology (equal); Software (equal); Validation (equal); Writing – original draft (equal); Writing – review & editing (equal). **Anita Verma**: Data curation (equal); Formal analysis (equal);

Investigation (equal); Writing – original draft (equal); Writing – review & editing (equal). **Thai-Son Nguyen**: Data curation (equal); Formal analysis (supporting); Investigation (supporting); Methodology (supporting); Software (supporting). **Len van Deurzen**: Data curation (supporting). **Yu-Hsin Chen**: Data curation (supporting). **Zhiren He**: Formal analysis (equal); Software (supporting); Writing – original draft (supporting). **Salva S. Rezaie**: Data curation (supporting); Formal analysis (supporting); Software (supporting); Writing – review & editing (equal). **Jakob Gollwitzer**: Data curation (supporting). **Benjamin Gregory**: Data curation (supporting); Software (supporting). **Suchismita Sarker**: Data curation (supporting); Formal analysis (supporting); Software (supporting). **Jacob Ruff**: Data curation (supporting). **Guru Khalsa**: Formal analysis (supporting); Software (equal); Writing – original draft (supporting); Writing – review & editing (supporting). **Andrej Singer**: Funding acquisition (equal); Investigation (supporting); Project administration (supporting); Resources (equal); Writing – review & editing (supporting). **David A. Muller**: Investigation (supporting); Project administration (supporting); Software (supporting); Supervision (supporting). **Huili G. Xing**: Conceptualization (supporting); Funding acquisition (equal); Investigation (supporting); Project administration (equal); Resources (supporting); Supervision (supporting); Writing – review & editing (supporting). **Debdeep Jena**: Conceptualization (lead); Funding acquisition (lead); Investigation (lead); Project administration (lead); Resources (equal); Supervision (equal); Writing – review & editing (equal). **Joseph Casamento**: Conceptualization (lead); Investigation (equal); Project administration (lead); Supervision (lead); Writing – original draft (supporting); Writing – review & editing (supporting).

DATA AVAILABILITY

The data that support the findings of this study are available from the corresponding authors upon reasonable request.

APPENDIX: MATERIALS AND METHODS

1. Epitaxial growth, in situ characterizations

ScN films were deposited at varying growth conditions on (0001) oriented Si-face 6H–SiC substrates using a Veeco® GenXplor molecular beam epitaxy (MBE) system with an idle-state base pressure of 5×10^{-10} Torr. A solid Sc source of 99.99% purity on a rare earth element basis from Ames Laboratory was supplied using a Knudsen effusion cell in the MBE environment. A molecular nitrogen gas of 99.999 95% purity was used with a growth pressure of ~10^{-5} Torr. The ScN films were grown without striking the nitrogen plasma, i.e., with 1.08 to 3.3 sccm molecular nitrogen gas and with Sc from an effusion cell, to evaluate the feasibility of ScN growth by self-activation. For reference, the ScN films were also grown with nitrogen plasma, wherein 1.95 sccm nitrogen was supplied with a Veeco® RF UNI-Bulb plasma source, and a RF plasma of 200 W was used. The ScN films were grown at various thermocouple substrate temperatures (at room temperature: 350, 550, 750, and 950 °C). Scandium was evaporated from a Knudsen effusion cell to get a Sc beam equivalent flux of 2.5×10^{-8} Torr. The films were grown in heavily nitrogen-rich conditions, where the Sc flux was less than molecular N_2 flux without plasma and less than the radical nitrogen (N^*) flux with plasma. The N^* flux is about two orders of magnitude smaller than the N_2 flux due to the finite efficiency of a plasma to generate N^* from N_2. Namely, Sc flux < N^* flux < N_2 flux in all cases of film growth presented here. Some ScN films were also grown at different Sc fluxes and N_2 flow rates. In addition to the 6H–SiC substrate, the ScN films were also grown on GaN and AlN template wafers. A metallic Sc film used as a reference for XPS analysis was grown by supplying Sc from an effusion cell and without flowing any nitrogen in the growth chamber at a substrate temperature of 550 °C and a chamber pressure of 4×10^{-9} Torr.

In situ monitoring of film growth was performed using a KSA Instruments reflection high-energy electron diffraction (RHEED) apparatus with a Staib electron gun operating at 14.5 kV and 1.45 A. In situ monitoring of the residual species in the growth chamber was performed by recording the mass spectra using a Stanford Research Systems (SRS) RGA100 series residual gas analyzer.

2. Lab-source and synchrotron-based x-ray diffraction measurement

After epitaxial growth, the film thickness, crystal structure, phase, and orientation were characterized using a Panalytical Empyrean® diffractometer at 45 kV, 40 mA, with Cu Kα1 radiation (1.540 57 Å). X-ray diffraction (XRD) symmetric 2theta-omega scans of the samples were collected with reciprocal space map (RSM) of the ScN 242, ScN twin 313, and 6H–SiC $\bar{1}015$ reflections. Symmetric skew phi scans of ScN 242 and 6H–SiC $\bar{1}015$ reflections were also collected. Film thickness and density were measured by x-ray reflection (XRR) spectra and compared to a simulated spectrum.

The high dynamic range mapping of a large volume in reciprocal Q-space was also performed with high energy x-ray scattering and a large area detector (Pilatus 6M detector from Dectris) at Cornell High Energy Synchrotron Source. The synchrotron beam's energy was tuned to 37 keV (wavelength ~0.335 Å) selected using a double-bounce diamond monochromator with a final spot size of 300 (V) × 800 (H) microns. For all films, we used the unique capability of QM2 Beamline for measuring the reciprocal space containing multiple Bragg reflections, allowing us to characterize several films rapidly. Using standard CeO_2 powder calibrations, geometric parameters of the Pilatus 6M detector, such as detector distance, titling, rotation, and direct beam position, were extracted. The large volume of 3D reciprocal space data was measured by phi rotation from 0° to 360° at room temperature.

3. HAADF-STEM measurement

The cross-sectional Scanning Transmission Electron Microscopy (STEM) samples were prepared using a standard lift-out process on a Helios G4 UX DualBeam focused ion beam system beam with a final milling voltage of 2kV of Ga ions. The Spectra 300 X-CFEG operating at 200 kV with a semi-convergence angle of 30 mrad and a High-Angle Annular Dark-Field (HAADF) detector with an angular range of 60–200 mrad was used to collect HAADF-STEM images. The HAADF-STEM images were acquired as a series of 25 images (250 ns per frame), cross-correlated, and subsequently averaged to produce images with a high signal-to-noise ratio. STEM energy-dispersive x-ray spectroscopy (EDX) data were collected using a steradian Dual-X EDX detector.

4. XPS (x-ray photoelectron spectroscopy) measurement

Film bonding and composition were analyzed with a Thermo Scientific Nexsa G2 x-ray photoelectron spectroscopy (XPS) instrument equipped with an Al Kα (1486.6 eV) source. Adventitious carbon and native oxide were removed from the sample surface using a 1 keV Ar^+ beam for 30 s. The photoelectrons were collected by a hemispherical analyzer with a pass energy of 58.7 eV. Prolonged high-resolution C1s, Sc2p, and N1s core level x-ray photoelectron spectra and N_{KLL} Auger electron spectra were collected to obtain a better signal-to-noise ratio. The spectra were analyzed using the CasaXPS software with a charge correction using C1s peak to 284.6 eV and spectral fitting, done with a combination of Lorentzian and Shirley background.

5. Raman, optical, AFM (atomic force microscopy) measurement

Raman spectroscopy was performed in a Witec system with a 488 nm wavelength excitation laser under normal-incident-normal-collection geometry. In the transmission geometry, ultraviolet and visible absorption spectra were measured using a Cary-5000-UV-Vis-NIR-Spectrometer system. Post-growth AFM measurements were performed using an Asylum Research Cypher ES system.

6. *Ab initio* growth pathways DFT calculations

Density functional theory (DFT) calculations were performed using the Vienna *Ab initio* Simulation Package (VASP),[50,51] with projector augmented wave pseudopotentials (Sc: $3s^2 3p^6 4s^2 3d^1$ and N: $2s^2 2p^3$), Perdew–Burke–Ernzerhof[52] exchange–correlation functional, and a kinetic energy cutoff of 520 eV. With the exception of isolated Sc and N atoms, all calculations are non-spin-polarized. Electronic convergence is reached when the difference in total energy is less than 10^{-7} eV between self-consistent steps, and structural relaxation is complete when the force on each atom is less than 10^{-3} eV/Å.

To obtain the energy of an isolated atom or molecule, it is placed in a large cubic cell, whose dimension is increased until there is no significant change (<5 meV) in total energy. A single k-point is used in these calculations. The results are $E_{Sc} = -2.107$ eV, $E_N = -3.125$ eV, and $E_{N2} = -16.666$ eV.

Cubic rock salt ScN consists of alternating Sc and N planes. The [111] growth at the ScN surface is referenced to an in-plane supercell containing a slab of ten atomic planes and at least 20 Å vacuum out-of-plane (Fig. S12). The in-plane dimension of the cell is $\left(\frac{\sqrt{6}}{2}a\right) \times \left(\frac{\sqrt{2}}{2}a\right)$, where a = 4.518 Å is the lattice parameter of the DFT relaxed conventional cubic rock salt cell of the bulk ScN crystal. For all slab calculations, we use a k-point mesh of $6 \times 8 \times 1$ and Gaussian smearing with a small smearing width of 0.02 eV. Only atoms near the top surface of the slab are relaxed. For slabs with a net dipole moment, we apply the dipole correction along the z-direction as implemented in VASP.[53] The growth is modeled by adding additional atoms (Sc, N) or N_2 molecules above the reference structure. To find intermediate metastable states, we first bring the atom or molecule in proximity to the top surface and relax all atoms near this surface. We then investigate possible energy barriers between the (meta)stable states through the nudged elastic band method,[54] with convergence achieved when the force (tangential + spring) on every atom of the images is below 0.01 eV/Å. The nitrogen plasmas are approximated as nitrogen atoms. This approximation neglects the kinetic energy of the nitrogen plasma, the generation of free radicals and ions, and other complexities related to the plasma. Qualitatively, we expect a larger energy drop in the nitrogen plasma growth pathway of Fig. 5, when these effects are included. This energy drop is likely even larger in growth techniques where the substrate or the plasma is electrically biased (e.g., sputtering, physical vapor deposition, etc.).

REFERENCES

[1] R. Kalescky, E. Kraka, and D. Cremer, J. Phys. Chem. A **117**, 8981 (2013).
[2] J. N. Galloway, F. J. Dentener, D. G. Capone, E. W. Boyer, R. W. Howarth, S. P. Seitzinger, G. P. Asner, C. C. Cleveland, P. A. Green, E. A. Holland, D. M. Karl, A. F. Michaels, J. H. Porter, A. R. Townsend, and C. J. Vorosmarty, Biogeochemistry **70**, 153 (2004).
[3] D. C. Rees, F. Akif Tezcan, C. A. Haynes, M. Y. Walton, S. Andrade, O. Einsle, and J. B. Howard, Philos. Trans. R. Soc. A. **363**, 971 (2005).
[4] L. Curatti and L. M. Rubio, Plant Sci. **225**, 130 (2014).
[5] B. M. Hoffman, D. Lukoyanov, Z.-Y. Yang, D. R. Dean, and L. C. Seefeldt, Chem. Rev. **114**, 4041 (2014).
[6] K. Eriguchi, Jpn. J. Appl. Phys. **56**, 06HA01 (2017).
[7] K. Eriguchi and K. Ono, Microelectron. Reliab. **55**, 1464 (2015).
[8] T. Ikeda, A. Tanihara, N. Yamamoto, and K. Eriguchi, J. Appl. Phys. **126**, 083304 (2019).
[9] J. Casamento, H. G. Xing, and D. Jena, Phys. Status Solidi B **257**, 1900612 (2020).
[10] D. Jena, R. Page, J. Casamento, P. Dang, J. Singhal, Z. Zhang, J. Wright, G. Khalsa, Y. Cho, and H. G. Xing, Jpn. J. Appl. Phys. **58**, SC0801 (2019).
[11] I. Akasaki, Rev. Mod. Phys. **87**, 1119 (2015).
[12] H. Amano, Rev. Mod. Phys. **87**, 1133 (2015).
[13] S. Nakamura, Rev. Mod. Phys. **87**, 1139 (2015).
[14] A. R. Smith, H. A. H. AL-Brithen, D. C. Ingram, and D. Gall, J. Appl. Phys. **90**, 1809 (2001).
[15] S. Kerdsongpanya, N. Van Nong, N. Pryds, A. Žukauskaitė, J. Jensen, J. Birch, J. Lu, L. Hultman, G. Wingqvist, and P. Eklund, Appl. Phys. Lett. **99**, 232113 (2011).
[16] D. Gall, I. Petrov, N. Hellgren, L. Hultman, J. E. Sundgren, and J. E. Greene, J. Appl. Phys. **84**, 6034 (1998).
[17] A. Le Febvrier, N. Tureson, N. Stilkerich, G. Greczynski, and P. Eklund, J. Phys. D: Appl. Phys. **52**, 035302 (2019).
[18] B. Saha, M. Garbrecht, J. A. Perez-Taborda, M. H. Fawey, Y. R. Koh, A. Shakouri, M. Martin-Gonzalez, L. Hultman, and T. D. Sands, Appl. Phys. Lett. **110**, 252104 (2017).
[19] M. A. Moram, S. V. Novikov, A. J. Kent, C. Nörenberg, C. T. Foxon, and C. J. Humphreys, J. Cryst. Growth **310**, 2746 (2008).
[20] L. Lupina, M. H. Zoellner, T. Niermann, B. Dietrich, G. Capellini, S. B. Thapa, M. Haeberlen, M. Lehmann, P. Storck, and T. Schroeder, Appl. Phys. Lett. **107**, 201907 (2015).
[21] S. Acharya, A. Chatterjee, V. Bhatia, A. I. K. Pillai, M. Garbrecht, and B. Saha, Mater. Res. Bull. **143**, 111443 (2021).
[22] M. A. Moram, Y. Zhang, M. J. Kappers, Z. H. Barber, and C. J. Humphreys, Appl. Phys. Lett. **91**, 152101 (2007).
[23] M. A. Moram, M. J. Kappers, Y. Zhang, Z. H. Barber, and C. J. Humphreys, Phys. Status Solidi A **205**, 1064 (2008).
[24] S. W. King, R. J. Nemanich, and R. F. Davis, Appl. Phys. Lett. **105**, 8 (2014).
[25] J. Casamento, J. Wright, R. Chaudhuri, H. G. Xing, and D. Jena, Appl. Phys. Lett. **115**, 172101 (2019).
[26] N. L. Adamski, C. E. Dreyer, and C. G. Van De Walle, Appl. Phys. Lett. **115**, 232103 (2019).
[27] B. Saha, G. V. Naik, S. Saber, C. Akatay, E. A. Stach, V. M. Shalaev, A. Boltasseva, and T. D. Sands, Phys. Rev. B **90**, 125420 (2014).

[28]M. Akiyama, K. Kano, and A. Teshigahara, Appl. Phys. Lett. **95**, 162107 (2009).
[29]M. Noor-A-Alam, O. Z. Olszewski, and M. Nolan, ACS Appl. Mater. Interfaces **11**, 20482 (2019).
[30]J. Casamento, H. Lee, T. Maeda, V. Gund, K. Nomoto, L. Van Deurzen, W. Turner, P. Fay, S. Mu, C. G. Van De Walle, A. Lal, H. G. Xing, and D. Jena, Appl. Phys. Lett. **120**, 152901 (2022).
[31]S. Fichtner, N. Wolff, F. Lofink, L. Kienle, and B. Wagner, J. Appl. Phys. **125**, 114103 (2019).
[32]J. Casamento, T.-S. Nguyen, Y. Cho, C. Savant, T. Vasen, S. Afroz, D. Hannan, H. G. Xing, and D. Jena, Appl. Phys. Lett. **121**, 192101 (2022).
[33]J. Casamento, K. Nomoto, T. S. Nguyen, H. Lee, C. Savant, L. Li, A. Hickman, T. Maeda, J. Encomendero, V. Gund, A. Lal, J. C. M. Hwang, H. G. Xing, and D. Jena, in *2022 International Electron Devices Meeting (IEDM)* (IEEE, 2022), pp. 11.1.1–11.1.4.
[34]J. Casamento, K. Nomoto, T.-S. Nguyen, H. Lee, C. Savant, L. Li, A. Hickman, T. Maeda, Y.-T. Shao, J. Encomendero, V. Gund, T. Vasen, S. Afroz, D. Hannan, D. A. Muller, H. G. Xing, and D. Jena, in *2023 IEEE BiCMOS and Compound Semiconductor Integrated Circuits and Technology Symposium (BCICTS)* (IEEE, Monterey, CA, 2023), pp. 132–136.
[35]N. Farrer and L. Bellaiche, Phys. Rev. B **66**, 201203 (2002).
[36]V. Ranjan, L. Bellaiche, and E. J. Walter, Phys. Rev. Lett. **90**, 257602 (2003).
[37]N. Takeuchi, Phys. Rev. B **65**, 045204 (2002).
[38]M. J. Winiarski and D. A. Kowalska, Sci. Rep. **10**, 16414 (2020).
[39]D. Kriegner, E. Wintersberger, and J. Stangl, J. Appl. Crystallogr. **46**, 1162 (2013).
[40]T. Henke, M. Knaut, C. Hossbach, M. Geidel, M. Albert, and J. W. Bartha, Surf. Coat. Technol. **309**, 600 (2017).
[41]H.-L. Kim, S.-W. Lee, Y.-S. Kim, D.-J. Kim, and W.-J. Lee, J. Korean Phys. Soc. **49**, 2418 (2006).
[42]M. D. Groner, F. H. Fabreguette, J. W. Elam, and S. M. George, Chem. Mater. **16**, 639 (2004).
[43]Y. K. V. Reddy, D. Mergel, S. Reuter, V. Buck, and M. Sulkowski, J. Phys. D: Appl. Phys. **39**, 1161 (2006).
[44]T. R. Paudel and W. R. L. Lambrecht, Phys. Rev. B **79**, 085205 (2009).
[45]S. Ahmad and N. Bouarissa, Mater. Res. Express **4**, 055001 (2017).
[46]R. Deng, B. D. Ozsdolay, P. Y. Zheng, S. V. Khare, and D. Gall, Phys. Rev. B **91**, 045104 (2015).
[47]B. Saha, J. Acharya, T. D. Sands, and U. V. Waghmare, J. Appl. Phys. **107**, 033715 (2010).
[48]A. K. Gupta and J. H. Leck, Vacuum **25**, 362 (1975).
[49]J. D. Haygood, D. M. Trayer, and R. F. Brown, *Arnold Engineering Development Center TR-69-109* (Arnold Air Force Station, Tennessee, 1969), pp. 1–67.
[50]G. Kresse and J. Furthmüller, Phys. Rev. B **54**, 11169 (1996).
[51]G. Kresse and D. Joubert, Phys. Rev. B **59**, 1758 (1999).
[52]J. P. Perdew, K. Burke, and M. Ernzerhof, Phys. Rev. Lett. **77**, 3865 (1996).
[53]J. Neugebauer and M. Scheffler, Phys. Rev. B **46**, 16067 (1992).
[54]H. Jonsson, G. Mills, and K. W. Jacobsen, *Classical and Quantum Dynamics in Condensed Phase Simulations* (World Scientific, 1998), p. 385.

Supplementary information

Self-activated epitaxial growth of ScN films from molecular nitrogen at low temperatures

Chandrashekhar P. Savant[1,a)], Anita Verma[1], Thai-Son Nguyen[1], Len van Deurzen[2], Yu-Hsin Chen[1], Zhiren He[3], Salva S. Rezaie[2,4], Jakob Gollwitzer[1], Benjamin Gregory[1], Suchismita Sarker[5], Jacob Ruff[5], Guru Khalsa[3], Andrej Singer[1], David Muller[2,4], Huili G. Xing[1,4,5], Debdeep Jena[1,2,4,5], Joseph Casamento[1,6,a),b)]

[1]Department of Materials Science and Engineering, Cornell University, Ithaca, NY 14853, USA.

[2]School of Applied and Engineering Physics, Cornell University, Ithaca, NY 14853, USA.

[3]Department of Physics, University of North Texas, Texas, 76203, USA.

[4]Kavli Institute at Cornell for Nanoscale Science, Cornell University, Ithaca, NY 14853, USA.

[5]Cornell High Energy Synchrotron Source, Cornell University, Ithaca, NY 14853, USA.

[5]School of Electrical and Computer Engineering, Cornell University, Ithaca, NY 14853, USA.

[6]Department of Materials Science and Engineering, Massachusetts Institute of Technology, Cambridge, MA 02142, USA.

[a)]Corresponding authors. Email: cps259@cornell.edu (C.P.S.); jac93@mit.edu (J.C.)

[b)]Present address: Department of Materials Science and Engineering, Massachusetts Institute of Technology, Cambridge, MA 02142, USA.

Self-activated growth of ScN films at different growth temperatures

Self-activated ScN film growth is demonstrated over a broad range of temperatures from room temperature to 950 °C, and they exhibit a similar RHEED diffraction pattern corresponding to twin cubic structure. A slight decrease in the lattice constant of <111> ScN films from ~4.514 Å to 4.496 Å is observed with the growth temperature from 20 ºC to 950 ºC.

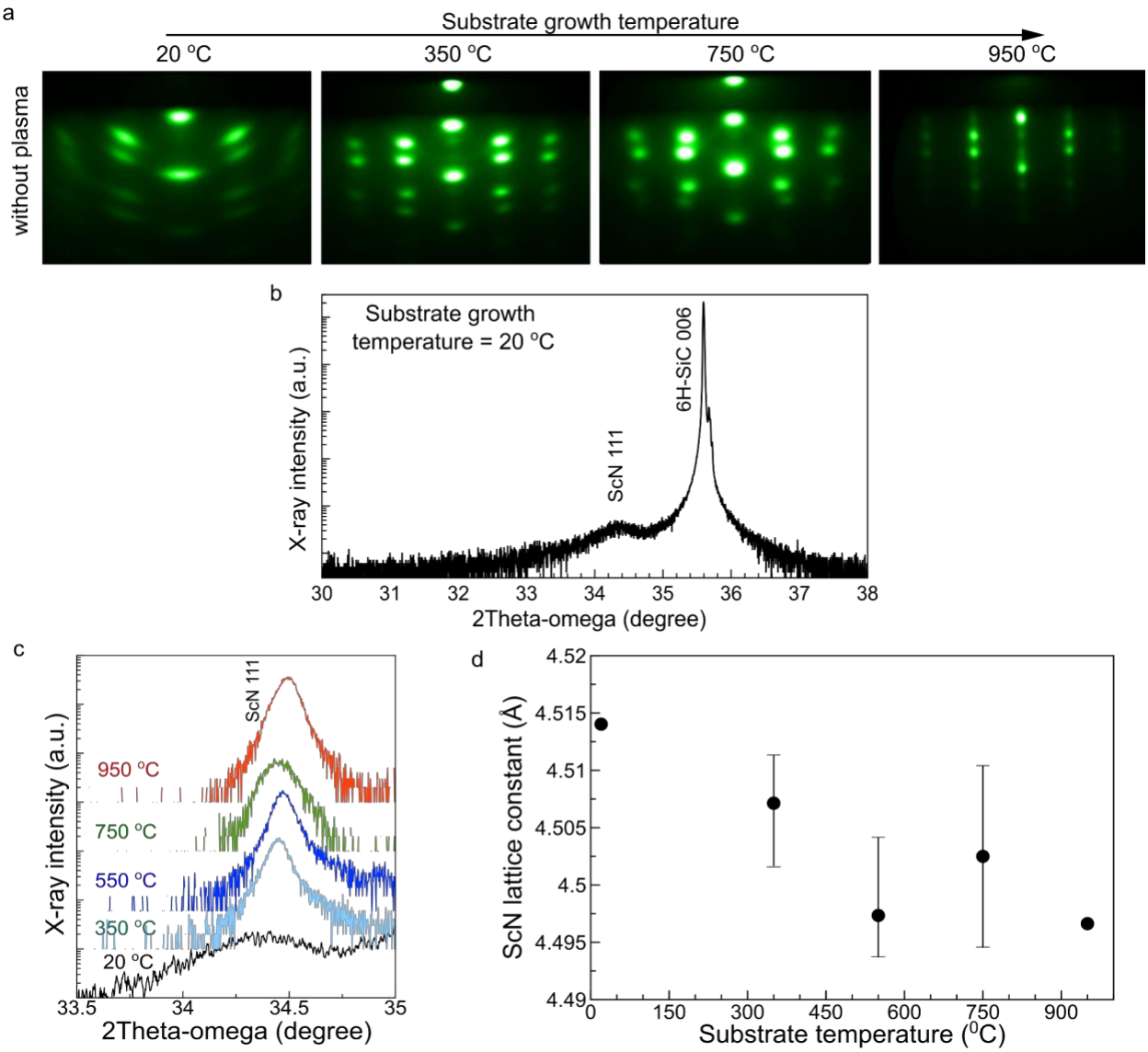

Figure S1. Self-activated growth of ScN films at different growth temperatures. a, RHEED diffraction pattern of ScN films grown without plasma on 6H-SiC at various substrate temperatures, b, XRD spectra demonstrating ScN film growth without plasma over a broad range of temperatures including at room temperature, c, ScN 111 Bragg reflections and, d, extracted lattice parameters of ScN film grown at substrate temperatures from 20 ºC to 950 ºC.

Extensive analysis of simulations and synchrotron-measured RSMs

Simulations and experimental measured RSMs are shown in Figures S3, S4, and S5. The experimental data was indexed with respect to the 6H-SiC substrate lattice parameters. As observed in experimental RSM patterns, the ScN thin film has in-plane Bragg reflection near the 6H-SiC substrate's Bragg reflections (i.e., ScN Bragg reflections are observed at ~0.97*H or ~0.97 *K to 6H-SiC substrate, where H/K=0,1,2…. n. These expected positions are estimated by the in-plane lattice parameter ratio of ScN and 6H-SiC ~3.08/3.189 = 0.97). While in the out-of-plane direction, ScN film peaks are observed at ~1.94*L with L=2n, where L=0,1,2…n, which matches well with estimated Bragg peak locations based on orientation and lattice parameter ratio (out-of-plane lattice parameter ratio = 15.10/7.811 ~1.94). However, the Bragg peaks of metallic Sc (Cyan box in figure (d)) are absent at Sc in-plane and out-of-plane direction at (3.08/3.3088) ~0.93*H or K and (15.10/ 5.2680) ~2.87*L, respectively, where H/K and L=0,1,2,..n. This indicates that measured 3D reciprocal space maps contain only multiple Bragg reflections related to the 6H-SiC substrate and ScN thin film.

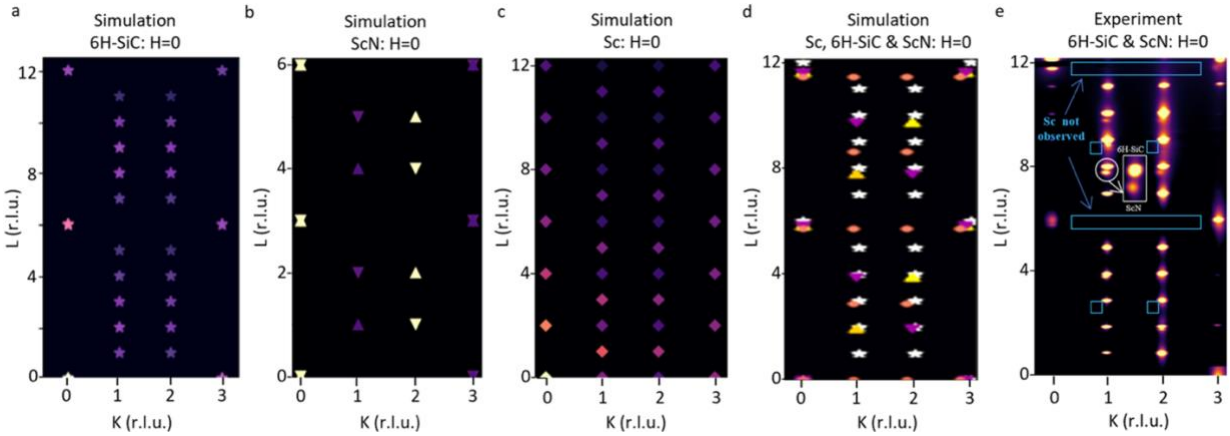

Figure S2. A comparison between simulations and experimental data in the H=0 plane for 6H-SiC, Sc, twin cubic ScN domains. a, Simulated diffraction pattern for 6H-SiC substrate with [0001] out-of-plane and $[01\bar{1}0]$ in-plane orientation. b, Simulated diffraction pattern for ScN film with twin (ABCA, and ACBA atomic layer stacking) cubic domains, Triangle up represents cubic ScN domain with [111] out-of-plane and $[2\bar{1}\bar{1}]$ in-plane orientation, triangle down represents another cubic ScN domain with [111] out-of-plane and $[\bar{2}11]$ (triangle down) in-plane orientation. c, Simulated diffraction pattern for Sc with [0001] out-of-plane and $[01\bar{1}0]$ in-plane orientation. d, A simulated diffraction pattern has been combined to depict the 6H-SiC substrate, ScN film, and ScN films with twin cubic domains, along with Sc. e, experimental diffraction pattern data shows multiple Bragg reflections for ScN film (grown without plasma at 550 °C) and 6H-SiC substrate and also shows metallic Sc is absent.

Table S1. In-plane and out-of-plane crystallographic orientation directions of 6H-SiC, Sc, ScN twin domains and their symmetry, space groups, and representation in simulated diffraction patterns in Figure S2a-c.

	Crystallographic axes			
Global axes	6H-SiC (Star) Hexagonal, Space group: $P6_3mc$	Sc (Diamond) Hexagonal, Space group: $P6_3/mmc$	ScN domain-1 (Triangle up) Cubic, Space group: $Fm\bar{3}m$	ScN domain-2 (Triangle down) Cubic, Space group: $Fm\bar{3}m$
x (h)	[0 1 $\bar{1}$ 0]	[0 1 $\bar{1}$ 0]	[2 $\bar{1}$ $\bar{1}$]	[$\bar{2}$ 1 1]
y (k)	[2 $\bar{1}$ $\bar{1}$ 0]	[2 $\bar{1}$ $\bar{1}$ 0]	[0 3 $\bar{3}$]	[0 $\bar{3}$ 3]
z (l)	[0 0 0 1]	[0 0 0 1]	[1 1 1]	[1 1 1]

Atomic layering sequence in twin cubic films

The different atomic layering sequences of the two twin domains of ScN and the 6-fold symmetric nature were analyzed using RSM slices at different L planes (Figure S3). The ScN thin films have a well-ordered crystal lattice with a 6-fold symmetry pattern, arising from discrete ABCA atomic layer stacking of one domain and ACBA stacking of the other twin domain.

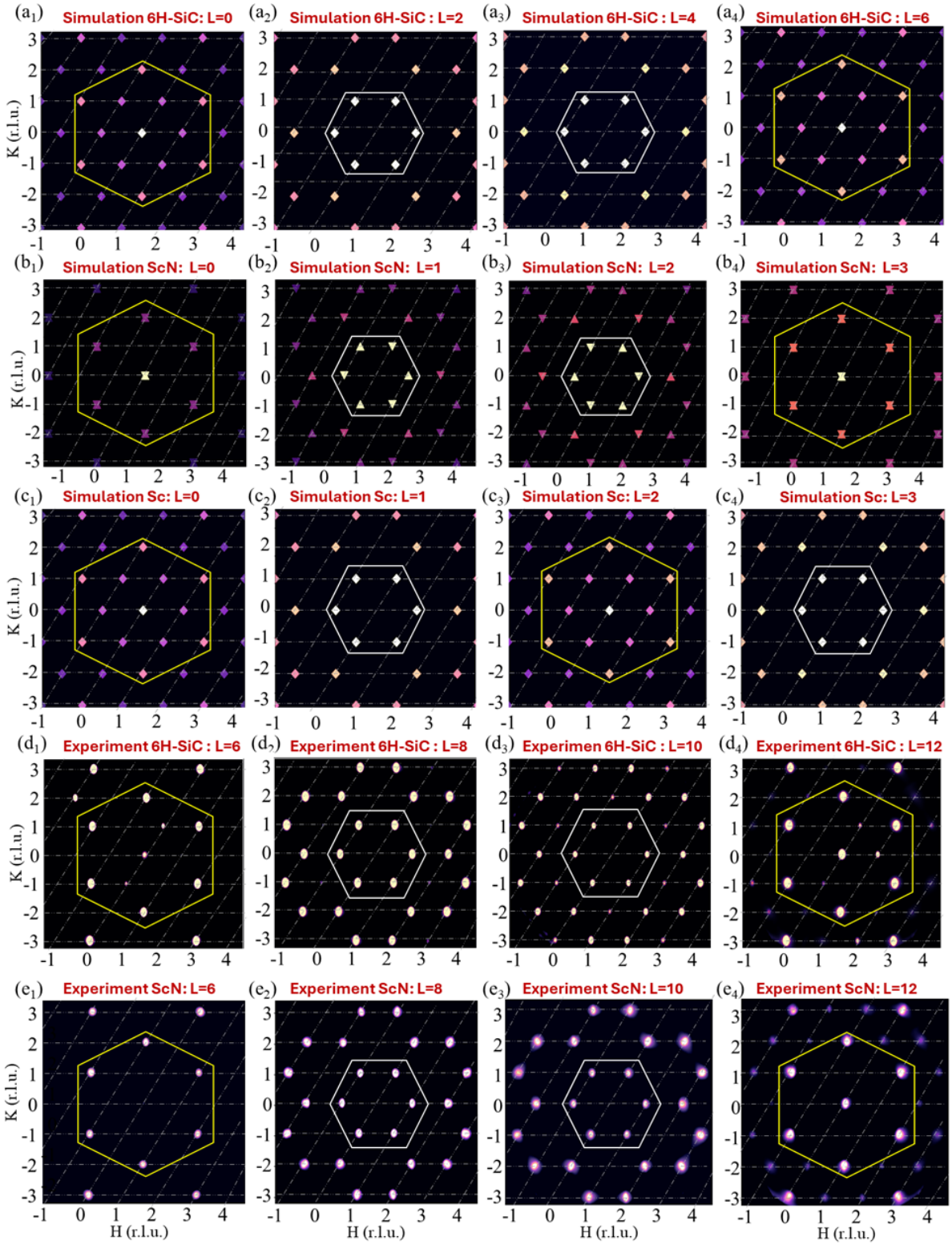

Figure S3. A comparison between simulated and experimentally measured 3D Reciprocal Space Map data for SiC-6H substrate and ScN (twin domains) thin film. a_1-a_4, Simulated diffraction pattern for 6H-SiC ([0001] out-of-plane orientation and $[01\bar{1}0]$ in-plane orientation) substrate at L=0, 2, 4, and 6 planes, respectively. The reflection pattern changes for every L=6n, where n=0,1,2---n. b_1-b_4, Simulated diffraction pattern for ScN film with twin cubic

domains at L=0, 1, 2, 3, and 4 planes, respectively. The square represents a cubic ScN domain with [111] out-of-plane orientation and $[2\bar{1}\bar{1}]$ (triangle up) in-plane orientation, circles represent another cubic ScN domain with [111] out-of-plane orientation and $[\bar{2}11]$ (triangle down) in-plane orientation. The reflection pattern changes for every L=3n, where n=0,1,2---n. c_1-c_4, Simulated diffraction pattern for Sc at L=0, 1, 2, 3, and 4 planes, respectively. The reflection pattern changes for every L=2n, where n=0,1,2---n. Experimental data shows substrate and film peaks overlapping at lower L values. Therefore, the data was compared at higher values of L. d_1-d_4, Experimental measured RSM shows multiple Bragg reflections for 6H-SiC substrate at L=6, 8, 10, and 12 planes, respectively. e_1-e_4, Experimental measured RSM shows multiple Bragg reflections for ScN thin film at L=6, 8, 10, and 12 planes for ScN film grown without plasma at 550 °C. As observed from simulated and experimental data comparison, the ScN thin film's in-plane Bragg reflections are present near the 6H-SiC substrate. While in the out-of-plane direction, the film peak is present (~ 1.93*L) near the substrate peak for an even number of L values.

Extensive Phase Purity analysis

Extensive phase purity analysis is performed by analyzing the entire large volume of the reciprocal space. Figure S4 shows RSMs over large reciprocal space averaged between H = (-0.3)-(0.3), 0.3-0.7, 0.7-1.3, 1.3-1.7, and 1.7-2.3. Only ScN twin cubic phase and 6H-SiC substrate reflections are seen. In comparison, no Bragg reflections are observed for any trace of secondary phases, such as metallic scandium or layered hexagonal ScN, etc., within the large volume of reciprocal space. This confirms the growth of phase pure twin cubic ScN films from molecular N_2 without plasma.

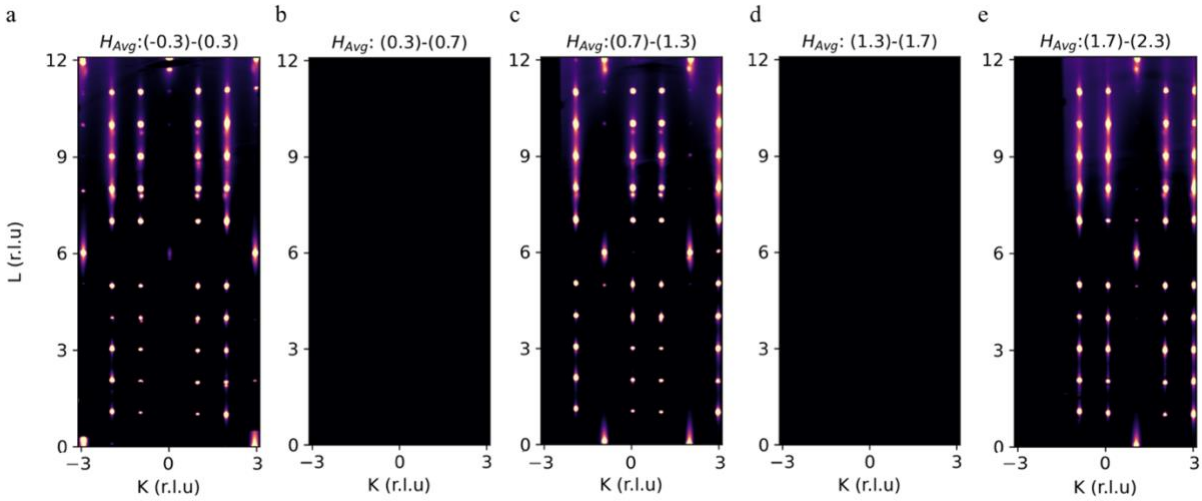

Figure S4. Extensive phase purity analysis of ScN films grown without plasma. a--e A Large Volume of Reciprocal space map measured by the Synchrotron X-Ray Scattering for ScN film grown without plasma at 550 °C on the 6H-SiC substrate, The measured 3D RSM averaged along the H values, where (a-e) H = (-0.3)-(0.3), 0.3-0.7, 0.7-1.3, 1.3-1.7, and 1.7-2.3 planes, respectively. Only ScN twin cubic phase and 6H-SiC substrate-related reflections are observed, suggesting that no secondary phase is present in the ScN films grown without plasma and confirming its phase purity.

Crystalline self-activated films

For the particular growth condition of 550 °C growth temperature and 2.5 × 10^{-8} torr Sc flux, the ScN film grown without plasma exhibits a high peak intensity with lower FWHM of 0.0865 r.l.u in out-of-plane direction when contrasted with ScN film grown with plasma (having FWHM of 0.179 r.l.u. in out-of-plane direction), as shown in Figure S5. Intense peaks with low FWHM indicate that the epitaxial ScN thin film grown without plasma has a high crystalline quality. It should be noted that the high crystalline quality observed for ScN grown without plasma is for the particular growth conditions mentioned above. Nonetheless, the self-activated ScN films show a pretty good crystallinity for growth temperatures from room temperature to 950 °C.

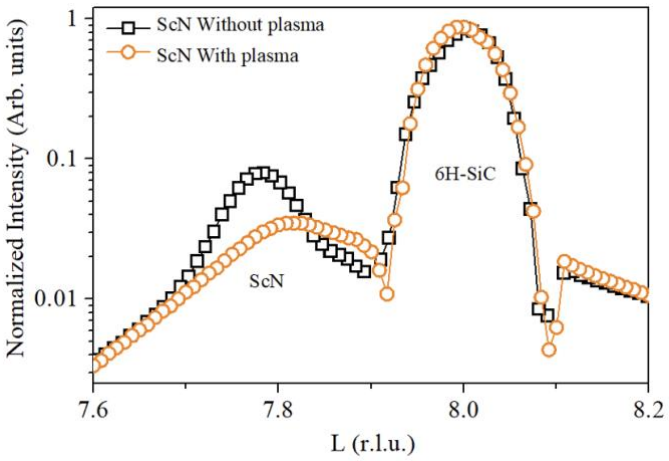

Figure S5. 1D line intensity plot for ScN film and 6H-SiC substrate Bragg reflection in the out-of-plane direction. ScN film grown without plasma has higher peak intensity with narrower FWHM than ScN film grown with plasma at 550 °C growth temperature.

HAADF STEM, EDAX and FFT analysis of Self-activated ScN films

It is well known that atoms can segregate at grain boundaries and other microstructural features, leading to local compositional inhomogeneity. Energy dispersive X-ray analysis (EDAX) was performed in the electron microscope to assess these potential effects and incorporate nitrogen in the grown films. Figure S6 shows a survey HAADF-STEM image and an EDX elemental map of the ScN film grown without plasma on a 6H-SiC substrate. The elemental map illustrates a uniform distribution of Sc and N throughout the film and does not show any local compositional inhomogeneities. The intensity depth profile, derived from the elemental maps, highlights a sharp interface between the film and substrate in this region.

Figure S7 (a and b) shows low-magnification HAADF-STEM images of ScN films grown with plasma and without plasma, respectively. The image contrast has been adjusted to emphasize the smooth surface on films grown with plasma (Figure S7a) and the pyramid facets on ScN films grown without plasma (Figure S7b). The smooth surface of the ScN film grown with plasma in Figure S7a is attributed to multiple rotated grains, as illustrated in Figure S7c from different regions of the films. The pyramidal surface morphology of the ScN film grown without plasma in Figure S7b is attributed to the larger and longer columnar twin domains that originated from the substrate surface and continue to the top of the ScN film, as illustrated in Figure S7d from different regions of the films. The ScN films grown without plasma exhibit larger columnar growth, as further evident in the line profile intensity shown in Figure S8.

Figure S8 presents the intensity line profile obtained from the HAADF-STEM images of ScN films grown with plasma (a, c) and without plasma (b, d) along the blue and red lines, respectively. The line spans a region of 1.5 nm. The intensity line profile of the ScN film grown with plasma displays oscillations corresponding to multiple rotated domains. Conversely, in the film grown without plasma, the intensity oscillates between alternating high and low intensities, revealing the presence of two twin domains.

Figure S9 displays the Fast Fourier Transform (FFT) of the ScN film grown without plasma. To determine the lattice constant of the film, we used the ideal lattice parameters of 6H-SiC with a = b = 3.1 Å and c = 83.3 Å. The pixel size of the FFT was measured based on the (030) diffraction spot. The lattice constant of ScN was then determined from its FFT pattern. The measured lattice constant for the ScN film grown without plasma is 4.3 Å, smaller than the relaxed value of 4.5 Å.

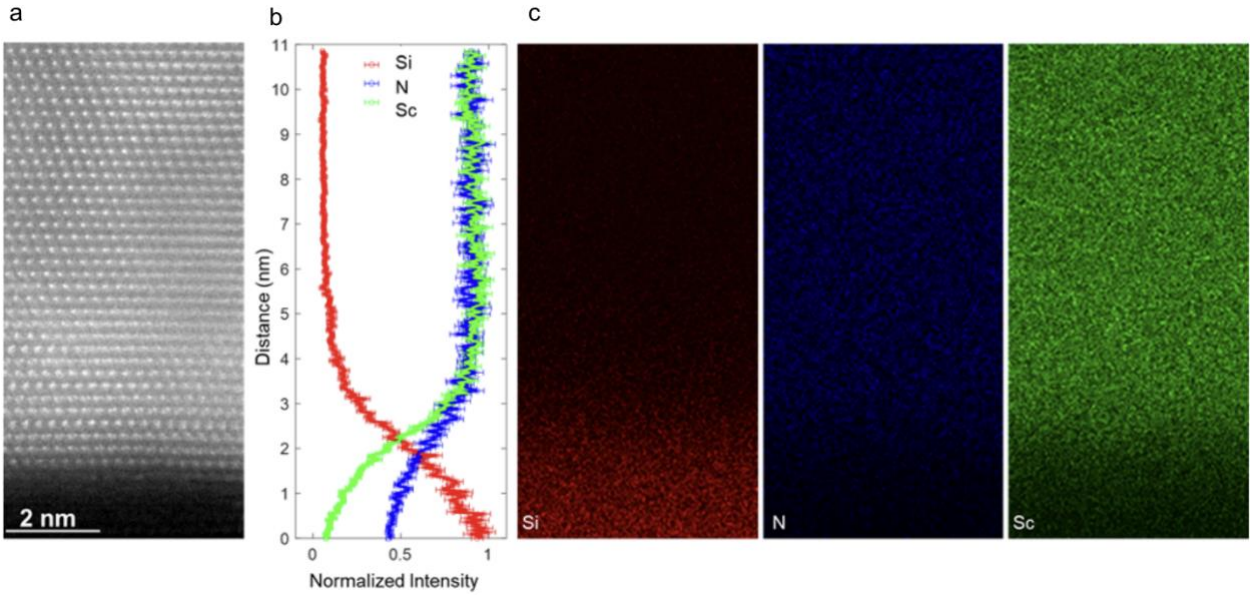

Figure S6. STEM-EDX Elemental Map of ScN Film Grown Without Plasma (a) Survey STEM image of the ScN film grown on 6H-SiC without plasma. (b) Elemental depth profile of EDX intensity for Si, N, and Sc. (c) STEM-EDS elemental mapping. The elemental map shows a uniform distribution of Sc and N in the ScN film.

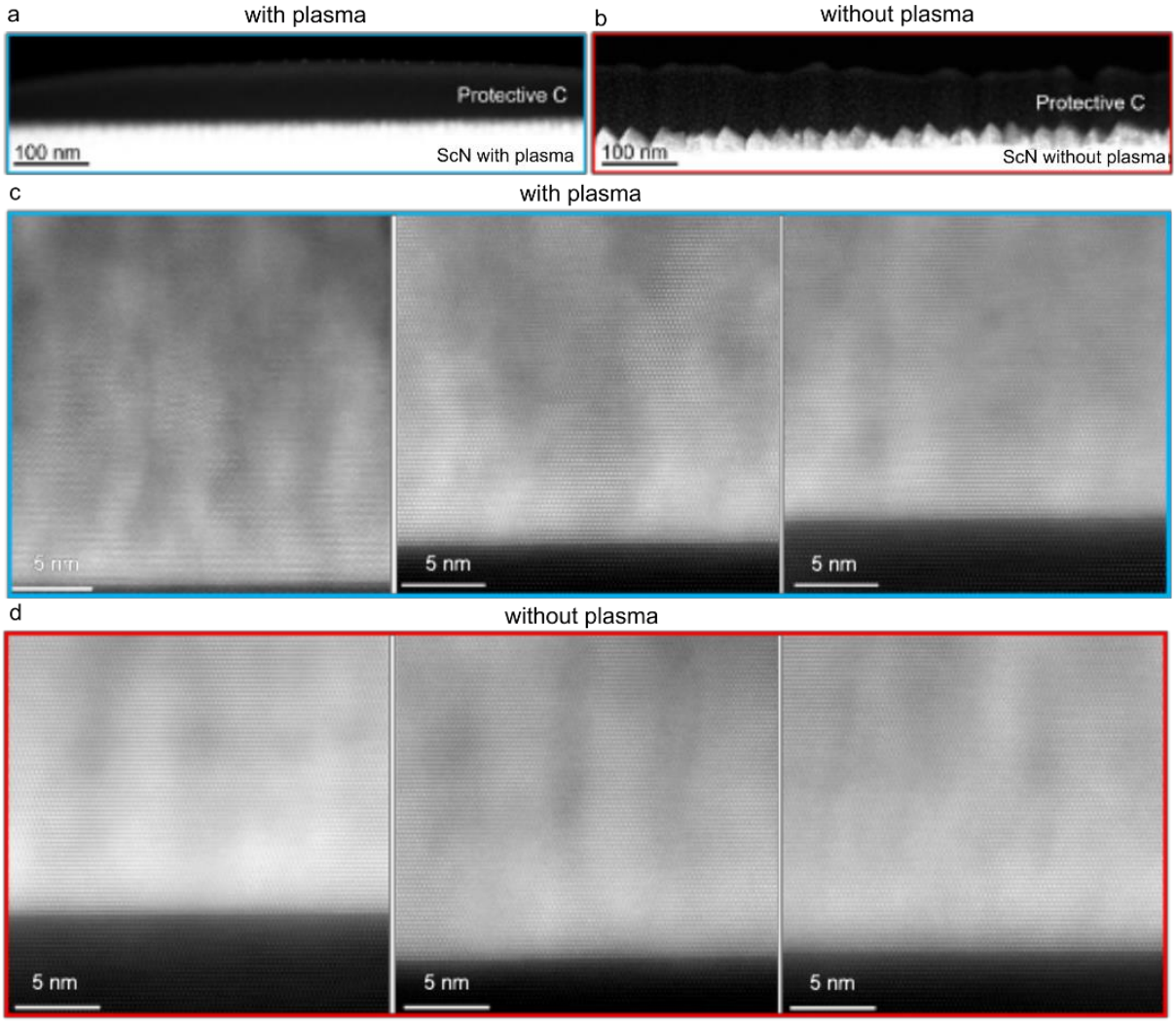

Figure S7. HAADF-STEM Images of ScN Films. (a) and (b) Low-magnification HAADF-STEM images of ScN films grown with plasma and without plasma, respectively. (c) and (d) Representative images of ScN films from different regions of films grown with plasma (highlighted in blue) and without plasma (highlighted in red).

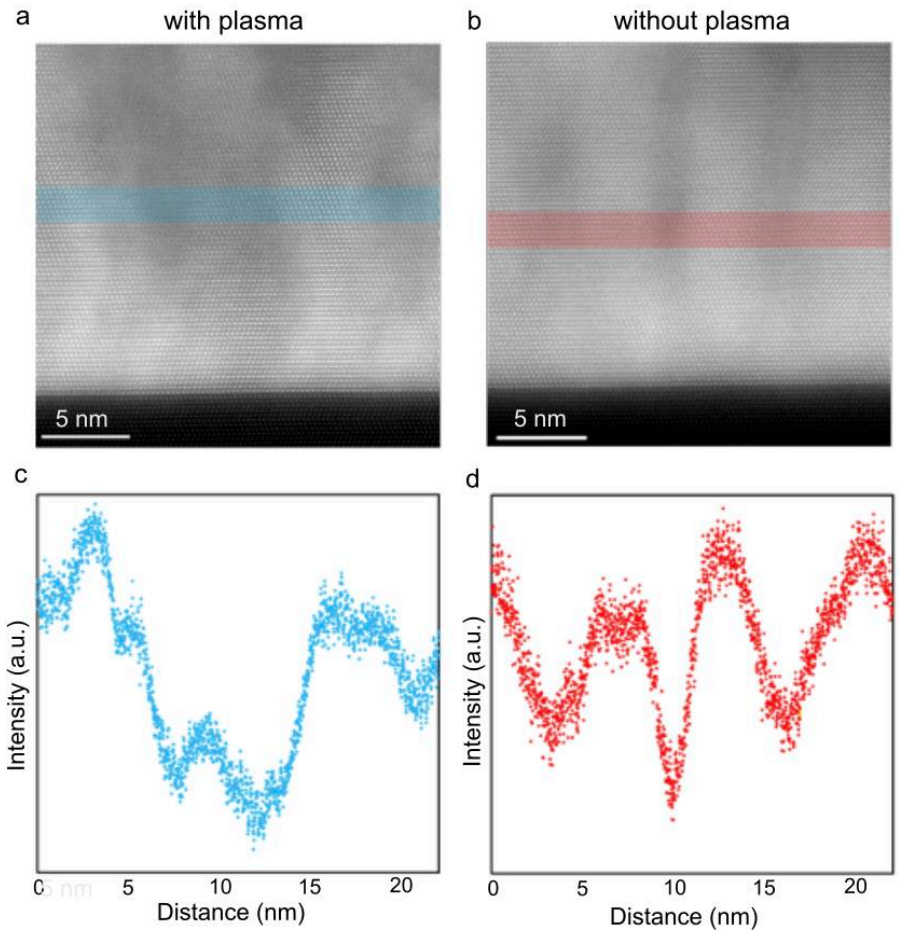

Figure S8. Intensity Line Profile of ScN Films. (a), (b) HAADF-STEM images of a selected ScN film grown with plasma, and without plasma, respectfully. (c) the intensity line profile along the red line for ScN film grown with plasma and along the blue line for ScN film grown with plasma, and (d) the intensity line profile along the red line for ScN film grown with plasma and along the blue line ScN film grown without plasma).

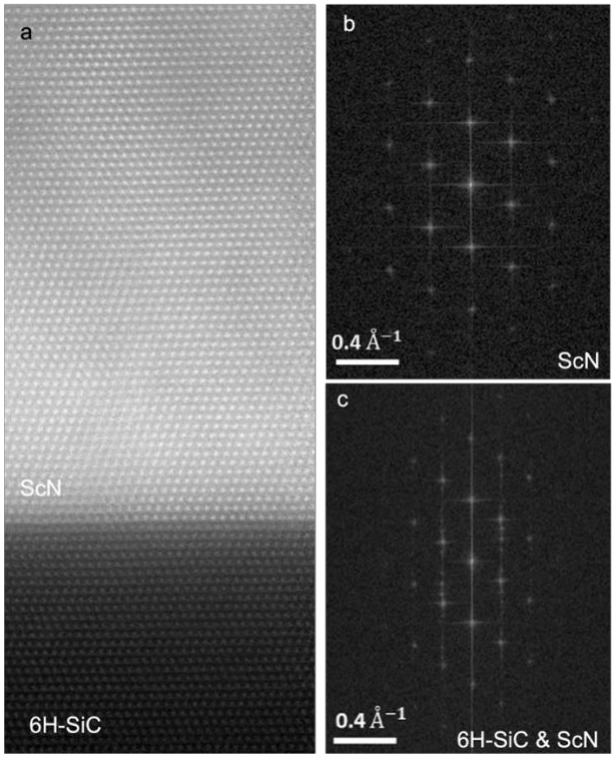

Figure S9. FFT Analysis of ScN Film Grown Without Plasma. (a) HAADF-STEM image of a selected ScN film grown without plasma, and associated FFT of the (b) film region only and (c) film and substrate combined.

Figure S10. Simulated color of ScN films. Uniformly integrated light from 740 to 565 nm (1.68 to 2.2 eV), yielding a brown-orange color in accordance with the transparency window of ScN in the visible regime and the resulting color of the ScN film.

Hall measurement data for the ScN films

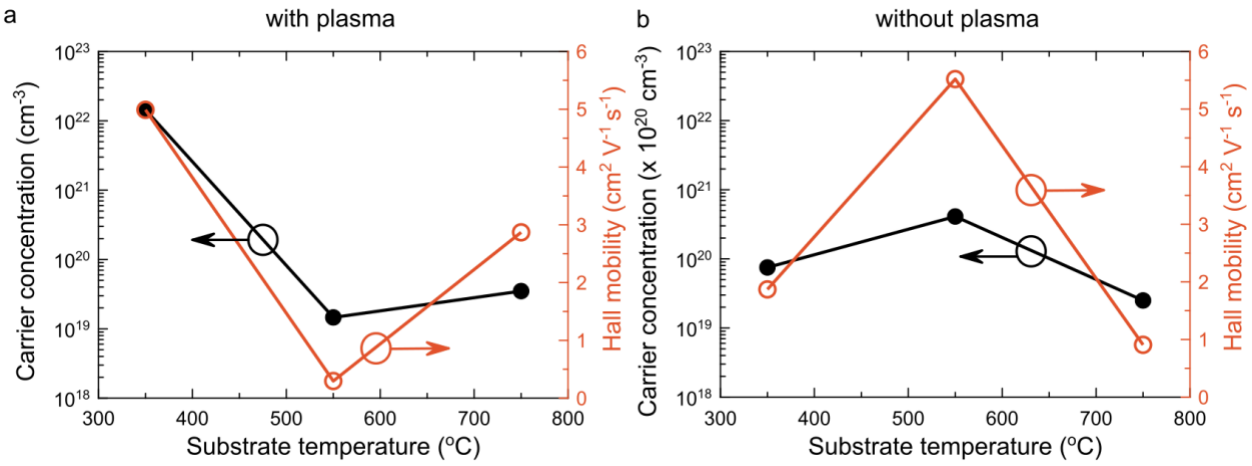

Figure S11. Hall measurement data for the ScN films. a, b, Room-temperature electron carrier concentrations and mobilities for ScN film samples grown at different substrate temperatures on 6H-SiC substrates, with plasma and without plasma, respectively.

Nudged elastic band results

Figures S12 and S13 show the minimum energy paths connecting the (meta)stable states obtained from nudged elastic band calculations. For the path in which an atom (or molecule) far away comes closer and eventually binds onto the surface, it is sufficient to start with a configuration where the atom (or molecule) is just 3 Å - 4 Å away from the surface, since beyond this distance the interaction between the atom (or molecule) and surface becomes weak.

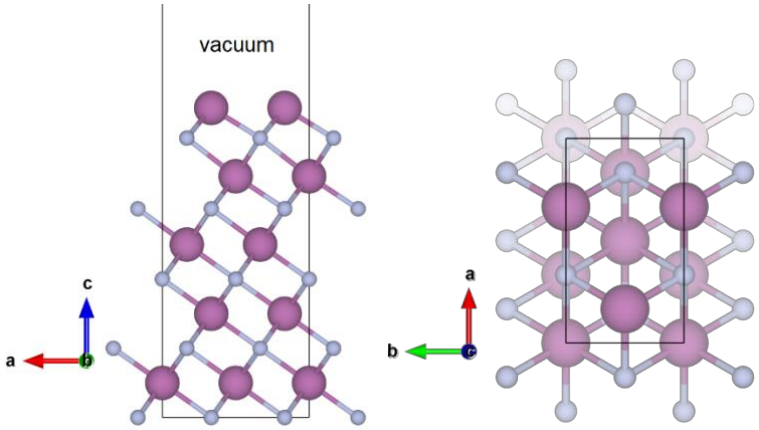

Figure S12. Side and top view of supercell used in ab initio calculation.

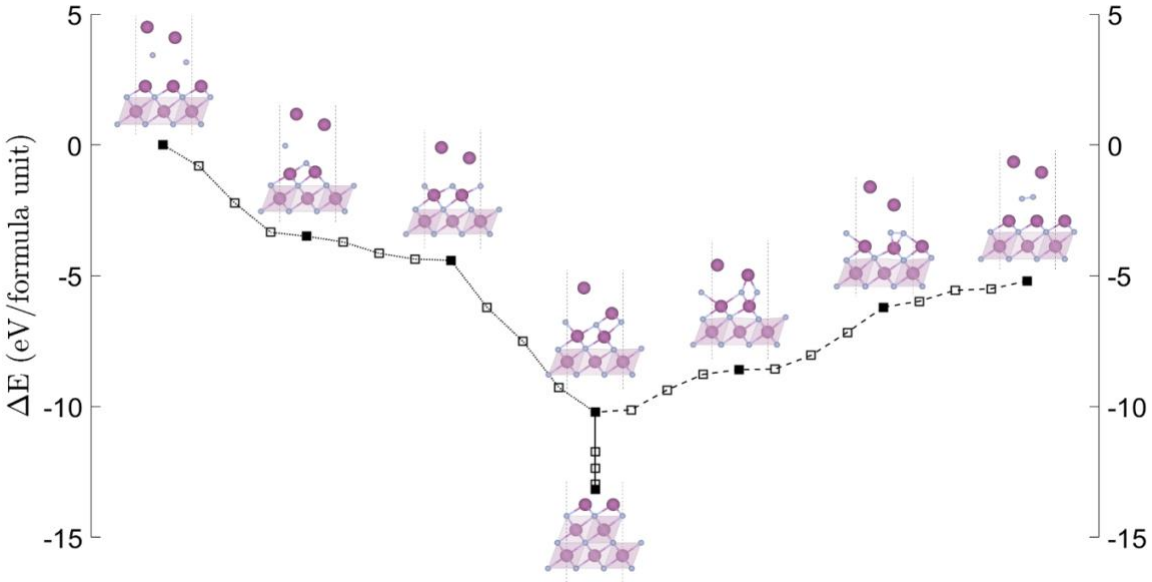

Figure S13. Nitrogen plasma and molecular N_2 growth pathways, including intermediate states. Solid squares represent the (meta)stable states, with unfilled squares representing the images connecting them. The dotted, dashed, and solid lines represent the nitrogen plasma path, molecular nitrogen path, and the shared path, respectively.

Scavenging effect of Sc on residual species in the MBE chamber

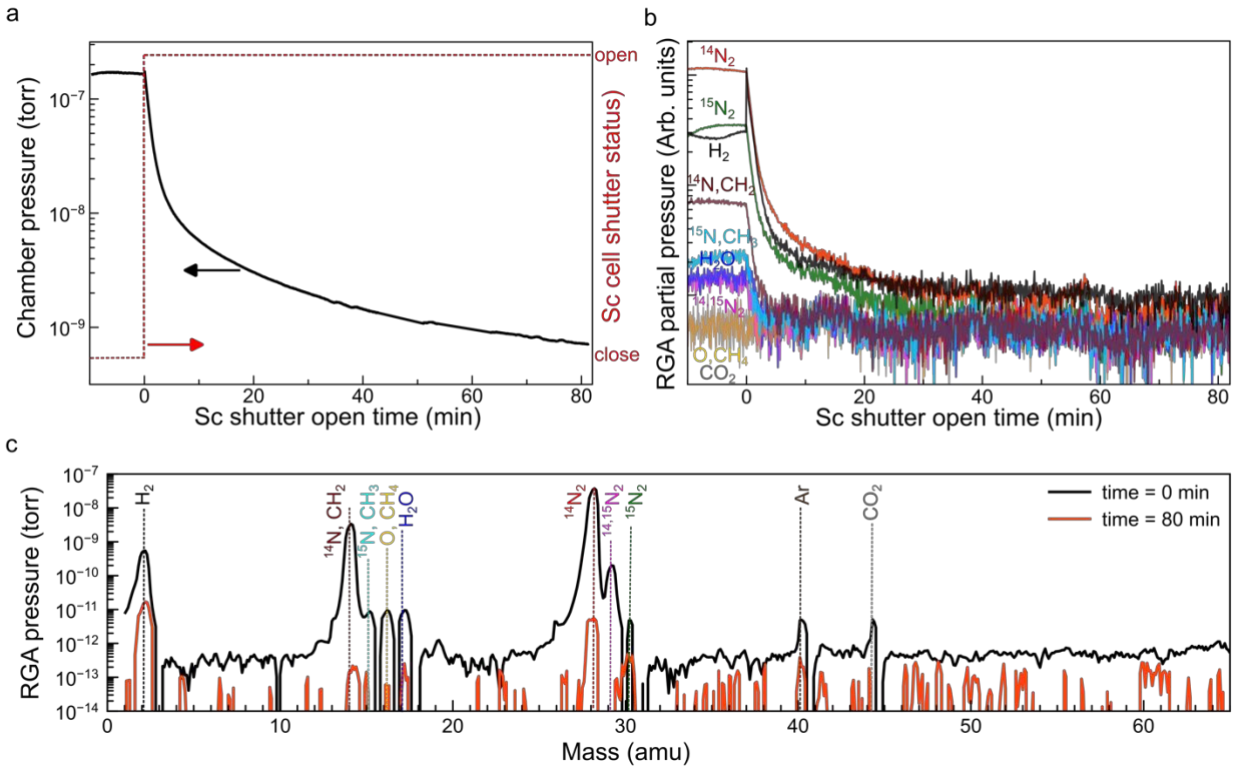

Figure S14. Scavenging effect of Sc on residual species in the MBE chamber. a, Chamber pressure **b,** Residual gas analysis (RGA) mass spectra taken before opening the Sc cell shutter (at t = 0 min) and after 80 min opening of Sc cell shutter. **c,** Residual gas analysis data for various species as a function of Sc effusion cell shutter open time (with Sc cell at 1408 ˚C, Sc flux at 3 × 10^{-8} torr). Sc flux is constant during the time when the chamber pressure continually decreases, indicating a gettering effect.

Demonstration of self-activated ScN film growths on different substrates and N_2, Sc flux

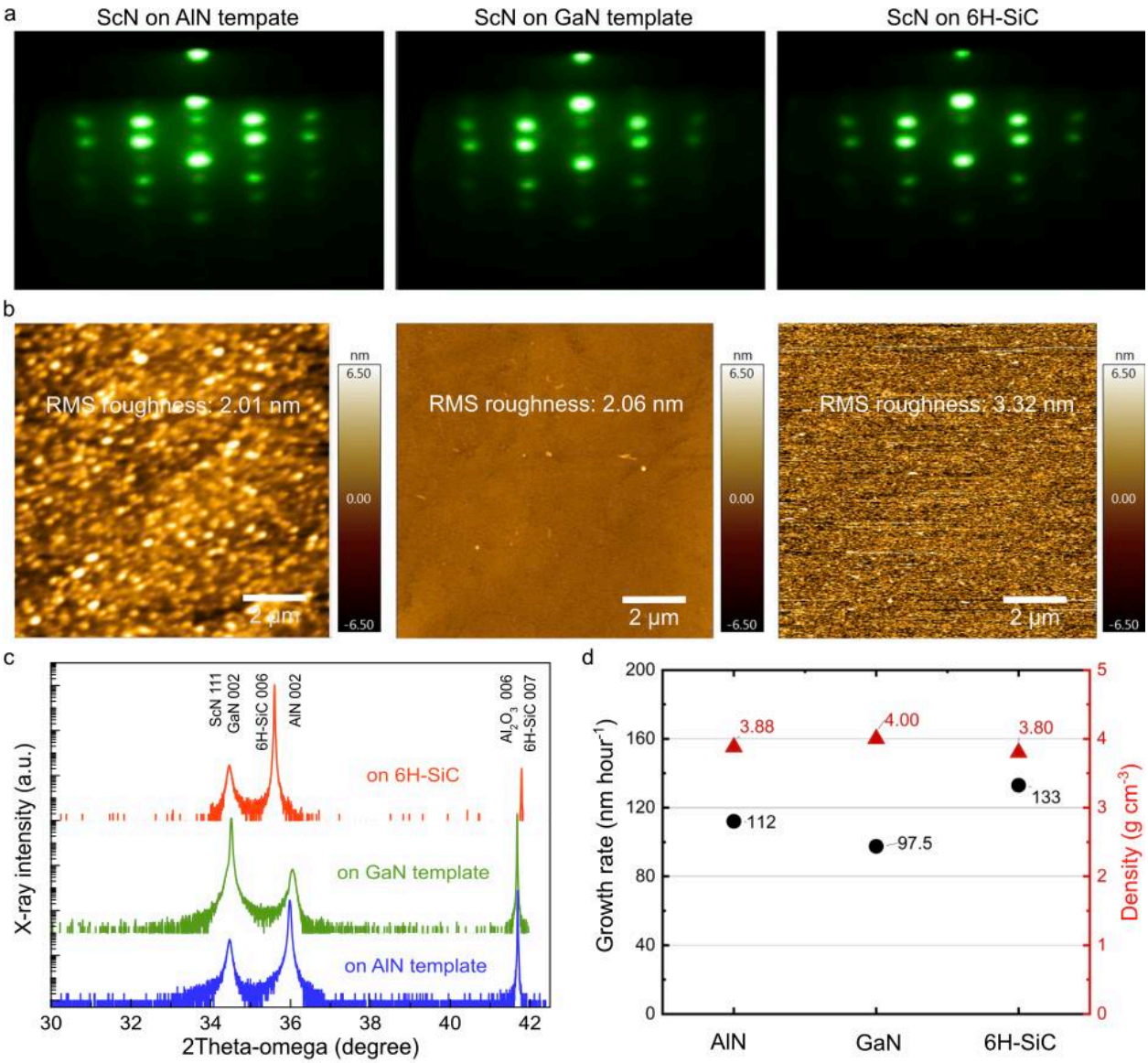

Figure S15. Demonstration of self-activated ScN film growths on different substrates. a, RHEED patterns, **b,** AFM micrographs **c,** X-ray diffraction spectra, and **d,** XRD Growth rates, densities of ScN films grown on various substrates (AlN, GaN, and 6H-SiC) without plasma, at substrate thermocouple temperature of 550 ℃, a Sc flux of 2.5 × 10^{-8} torr, and a nitrogen flow rate of 3.3 sccm.

Table S2. Growth rates of ScN films grown on 6H-SiC substrate without plasma at different Sc fluxes and nitrogen flow rates. ScN growth rate increases with Sc flux but not N_2 flux, suggesting that the growths were Sc-limited and not limited by the availability of active N species.

Substrate Temperature (^oC)	Sc flux (10^{-8} torr)	N_2 flow rate (sccm)	Growth Rate (nm hour^{-1})
550	0.8	3.3	17
550	1.5	3.3	61
550	3	3.3	151
550	3	1.08	154